Flexible Colloidal Quantum Dot Photodetection with Cellulose Structures

Jingda Wu

A dissertation submitted in partial fulfillment of the
requirements for the degree of

Doctor of Philosophy

University of Washington

2016

Reading Committee:

Lih Y. Lin, Chair

Arka Majumdar

Manjari Anantram

Qiuming Yu

Program Authorized to Offer Degree:
Electrical Engineering

University of Washington

Abstract

Flexible Colloidal Quantum Dot Photodetection with Cellulose Structures

Jingda Wu

Chair of the Supervisory Committee:
Professor Lih Y. Lin
Electrical Engineering

This thesis will outline a new way of fabricating flexible photodetectors. Solution-processable colloidal quantum dots (QDs, or nanocrystals(NCs)) are incorporated into cellulose structures to form a composite structure that can be used for photodetection. This enables new ways of device fabrication and also makes ultrathin, ultraflexible and even transparent optoelectronic devices possible.

Inkjet printing with an office inkjet printer is introduced and applied towards PEDOT:PSS transparent electrode deposition. This offers a low cost method for material deposition. Flexible photoconductors are fabricated with these electrodes and CdSe quantum dot embedded tracing paper by utilizing the porous cellulose structure. Consistent photoresponse is achieved with such a structure under 550nm light illumination.

After further realizing the shortcomings of tracing paper for its large thickness and low porosity, which both deteriorate the performance of these devices, natural plant-membranes are chosen as an alternative and offer superb properties for optoelectronic device fabrication. Visible-blind self-powered ultra-violet detectors are designed and fabricated with the incorporation of ZnO QDs on reed membrane. Schottky junction devices are fabricated with the use of gold and aluminum as the electrodes. Sub-second responses are observed at a bias of zero, which is superior than most of the flexible photoconductors in the literature. An external quantum efficiency of over 3% is discovered

with the device at 350nm light illumination under zero bias. A great performance enhancement is also observed on the devices fabricated on reed membrane comparing to the ones on tracing paper.

Nanofibrillated cellulose(NFC) can be readily used to fabricate transparent papers. ZnO QD-NFC composite structure is prepared and fabricated into ultrathin transparent papers with a thickness less than 1 micrometer. Self-powered Schottky photodiodes are fabricated on such papers and relatively fast response is observed at zero bias.

TABLE OF CONTENTS

Page

LIST OF FIGURES

LIST OF TABLES

Table Number Page

ACKNOWLEDGMENTS

This work would not have been possible without the support, help and collaboration from many people.

I would first like to thank my academic advisor Lih Y. Lin for giving me the opportunity to do this research and her enormous support. I am thankful for the freedom I had to explore flexible device area and the guidance I received to shape my research. There are a lot of times I made mistakes, times I got emotionally upset and times I was unproductive, but she was always very patient and helped me through. I also greatly appreciate the opportunities she gave me to work on optical tweezers project and MEMS resonator project, from which I learned a lot and enjoyed collaboration with other group members.

Additionally, I would like to thank the other members of my committee. I have a lot of beneficial chats with Arka Majumdar and Manjari Anantram, which not only helped my research, but also on personal development. Thank Qiuming Yu, whose students I have a lot of happy collaborations with, for being in my committee. Thank Peter Pauzauskie for serving as the graduate school representative.

I would also like to thank some of my friends who had helped me a lot on the projects: Jiayi Dou, who helped me on microfluidizing; Long Gui and Lige Tonggu, who helped me on TEM imaging and other equipment; Guanqun Luo and Chang Dou, whom I had a lot of helpful discussions with on paper making and material characterization.

I would like to thank the past and present members of Lin group: Erin Sanehira, Ethan Keeler, Yu Jin, Conner Ballew, Peifeng Jing, Matt Strathman, Cameron Simmons, Yunbo Liu, Chang-Ching Tu, Chen Zou, Ji Hoo and Jiang Nan. I feel so lucky to be within such a collaborative, supportive and enthusiastic environment. We also had a lot of fun hanging out and learning about all kinds of stuff.

Special thanks to Thessalonika Benny, who’s my family stay host on the first several days when I came to the US. At a time when I lost contact with my friend, it was T who gave me somewhere to stay. Needless to say all the things about this totally strange country I learned from her. Also I need to thank Kai Wei and Hui Chen, whom I was on the same flight with that introduced me to T and became my first friends at the US.

Finally, I would like to thank all my other friends, my parents and relatives for their support throughout the years.

Chapter 1

INTRODUCTION

Flexible device has risen to be an important research topic in the recent twenty years due to a variety of advantages over devices with rigid structure. Large-scale, facile, and low-cost fabrication methods are enabled with the incorporation of low-cost and easy-to-synthesis solution-processable materials. Its superb integratibility also drives the commercialization potential for wearable, foldable and roll-up devices such as displays, solar cells and sensors.

Photodetection has been an inseparable part of daily life. Most of today's smartphones have integrated cameras, ambient light sensors and infrared sensors for different purposes of use. It's also been used for optical communication, environmental monitoring and medical detection. Despite the mature industry behind all these applications, the development of flexible photodetectors is still at its infancy. Apart from the advantages for general flexible devices, curved photodetectors [1], especially for imaging purpose, withal helps to compensate for lens aberration and provide sharper and clearer results. This is extremely helpful when the lens system is very compact due to limited space for detection, such as portable devices and optical coherence tomography. Hence flexible photodetector is an important direction for flexible devices. Furthermore, the research on flexible photodetector is also beneficial for other optoelectronic devices that share similar device structures, such as solar cells and displays.

While inorganic materials such as silicon, germanium, gallium arsenide, etc., have been applied for optoelectronic applications for a long time. They are conventionally in bulk and the lack of flexibility prohibits them from using in applications for flexible devices, in spite of their high performance in electronics. This is where organic materials come into play and later dominates the area. However, inorganic semiconductor colloidal nanocrystals, a.k.a. quantum dots (QDs), work as an alternative by offering the same solution-processability for large-scale and flexible device fabrication, thanks to their availability through wet-chemistry synthesis, which offers organic-like behavior [2] to inorganic materials. Due to their small sizes, QDs are typically consist of much lesser atoms than their bulk brothers and thus behave more like an atom, i.e., stronger carrier confinements are present in QDs. Hence their bandgaps are determined by their size with smaller QDs having wider bandgaps. Much higher exciton binding energies are also found in QDs due to stronger electron-orbital interactions and thus improving the optical yields. [3, 4] Due to abrupt stops of lattice growth on the surface, QDs have a lot of dangling surface electron orbitals. With a high surface-to-volume ratio, these orbitals can be used for functionalization by modifying with functional groups. Nevertheless, unlike inorganic nanocrystals, complicated change of composite is needed to tune optoelectronic properties of organic materials. A great selection of well-studied inorganic semiconductor materials also provides advantages to apply them towards flexible applications. Typically CdSe and ZnO QDs are studied extensively.

With all these being said, the integration of nanomaterials with flexible substrates is not fully researched. For devices with vertical structures, it's typical that high quality, smooth films are needed to prevent short-circuiting problem, which requires engineering of materials, deposition methods and substrate. Typically spin-coating are used for solution-processable material deposition, but it wastes a lot of materials and also needs good control of the viscosity of the materials that are being used. Ink-jet printing turns out to be a promising material deposition method with minimal material consumption and direct patterning feature. However, the quality of the printing also depends a lot on the substrate and material. While polyethylene terephthalate (PET) and thin-film glass are used widely for flexible devices, it's still difficult to deposit high quality films on them without modification. We are able to modify a desktop inkjet printer to do PEDOT:PSS (poly(3,4-ethylenedioxythiophene) polystyrene sulfonate, a conductive polymer) printing on unmodified transparency films, which are used for class room presentations. But the high roughness of the printed films caused short-circuiting when using these films for devices. In order to prevent this problem and still use these low-cost material deposition method, we introduced an interspacing layer consists of cellulose structures. Typically tracing paper are smooth and semi-transparent, which is good for optoelectronic applications, and are applied towards photovoltaic circuits as a substrate [5]. But we figured that it can also be used as the interspacing layer by incorporating QDs. The first generation of devices used a sandwiching structure with a CdSe QD embedded tracing paper between two ink-jet printed PEDOT:PSS electrodes on unmodified transparency films. This device functions as a photoconductor and an increase of device performance is observed with the device under bending.

While tracing paper is common and of low-cost, its large thickness ($>$30 μm) and low porosity limits the conduction path of QDs and thus deteriorate the performance of the devices. Therefore thinner and more porous materials are needed for interspacing purpose and we found reed membrane is a good candidate with about 5μm thickness and relatively large porosity due to its nature of nutrition transportation. ZnO QDs are synthesized and embedded into the membrane to act as the active layer. In order to improve the response speed and carrier extraction of the device, metal electrodes are directly evaporated onto the membrane to improve metal/ZnO QD contacts. A Schottky photodiode structure is introduced with gold to be the anode and aluminum the cathode and we demonstrated a self-powered flexible UV photodetector that has an external quantum efficiency(EQE) of $>$3% under 350nm light illumination at zero bias.

However, either tracing paper or reed membrane is still much thicker than the active material layer of traditional thin film devices, which is typically of 100s of nm. Both of them have rough surfaces that are not ideal for device applications. Their formation is established and cannot be modified without damaging the structure. Therefore we looked into making our own cellulose structures starting from cellulose fibers. Nevertheless, most of the natural celluloses and common papers are made of micro-sized celluloses, i.e. celluloses with diameters in micrometer scales, and makes it difficult to get thin papers due to poor material strength. Disintegration of these celluloses will result in primitive cellulose fibers which are of nanometer scales that can be used to make much thinner, transparent and strong papers that are ideal candidate for optoelectronic applications [6]. TEMPO-mediated oxidation and high energy microfluidizing processes are also introduced to make nanofibrillated cellulose (NFC). ZnO QDs are readily mixed with NFCs and filtered to form a thin film paper wet gel. By drying the gel, a freestanding fluorescent thin film can be achieved. In order to further reduce the thickness of the film, we introduced a solvent exchange process with the wet gel soaking in isopropanol to reduce the capillary force from water and thus to freestand ultrathin ZnO QD-NFC films. The film has $>$97% transparency in visible light range and a thickness of $<1\mu$m. Electrodes are evaporated onto the film and we are able to make devices with different structure. Fast response devices are achieved with the same structure as the reed membrane device. High EQE is observed on devices with MoO_3 layer insertion.

This thesis consists of six chapters. Chapter 1 is about the motivation of why I am working on flexible nanocrystal photodetection and a brief introduction of what I did. Chapter 2 is about the backgrounds of my research topic. It will include basics about colloidal QDs and cellulose structure. Chapter 3 talks about the flexible CdSe QD detectors I made on tracing paper with inkjet printed electrodes on transparency films. Device design and device performance will be discussed. Chapter 4 is on ZnO QD-based Schottky photodiode on reed membrane and Chapter 5 on ultrathin ZnO QD-NFC composite membrane based photodetector. I'll draw a conclusion in Chapter 6 on my PhD work and propose some future work.

Chapter 2

BACKGROUND

2.1 Colloidal Nanocrystal Quantum Dots

2.1.1 Introduction

Colloidal nanocrystal quantum dots (CQDs) (Figure 2.1) are nano-sized semiconductor particles that can be synthesized through wet-chemistry methods and suspend in solution, which is a key difference from QDs fabricated through molecular beam epitaxy (MBE). The property thus offers solution-processability for facile and low-cost fabrication methods such as printing, spin-coating and drop-casting. Unlike bulk semiconductors, QDs appear to have atomic-like behaviors because they are formed by a limited number of atoms. The electron wavefunction overlapping is not dense enough to form continuous energy band and QDs have discrete energy band, i.e., the energy band is quantized. Quantum wells and quantum wires also have discrete energy bands. The electrons are confined in one or two dimensions for these materials and free to move in the dimensions that are not confined. However, for QDs, the electrons are confined in all three spatial dimensions and thus have strong Coulomb coupling between carriers, which significantly enhances the optical property and is potentially promising for optoelectronic applications.Thanks to the advantages mentioned above, CQDs have been applied to numerous device applications, such as light emitting devices [7–10], photovoltaics [11–14], photodetectors [15–18] and transistors [19, 20], etc.

2.1.2 Band Structure

Ideally, quantum dot can be of any semiconductor when its size reaches the Bohr exciton radius of that material, which is the natural length of an exciton, of the material. In general, the Bohr radius

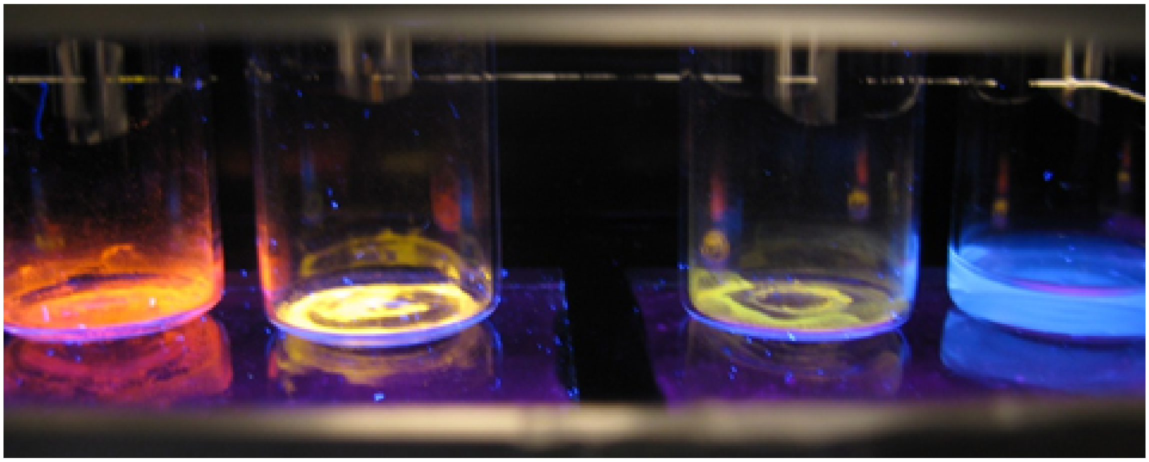

Figure 2.1: Silicon colloidal quantum dots of different sizes in solution form.

is given by

$$a_B = \epsilon \frac{m_e}{m^*} a_0, \tag{2.1}$$

where ϵ is the dielectric constant of the material, m_e is the rest mass of an electron, m^* is the reduced mass of electron and hole, and a_0 is the Bohr radius of the hydrogen atom, which is 5.29×10^{-11}m.

To understand the size-dependence of the energy band, we can simplify the QD system into a particle-in-a-sphere problem [21]. The spherical potential well of the sphere with a radius of a can be written as

$$V(r) = \begin{cases} 0, & r < a \\ \infty, & r > a \end{cases}, \tag{2.2}$$

The simple single particle Hamiltonian can be written as

$$H = -\frac{\hbar^2}{2m} \nabla^2 + V(\vec{r}), \tag{2.3}$$

which only has contributions from the kinetic energy(first term) and the potential energy(second term), with $\hbar$ the reduced Planck's constant. By solving this system under spherical coordinate, we can get the corresponding energy of the particle as $E_{n,l} = \hbar^2 \alpha_{n,l} / 2m_0 a^2$. α is a Bessel function related term which is discrete under the assumption. Thus the energy states of the particle is

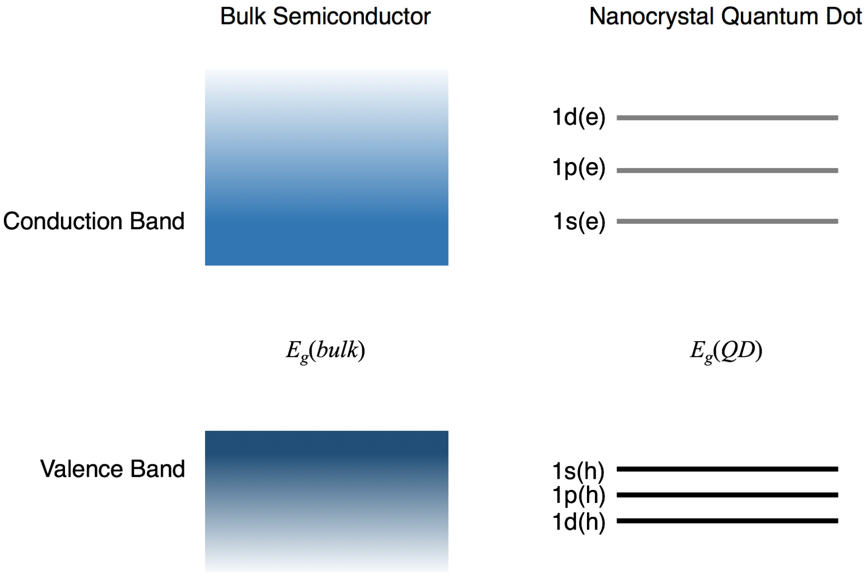

Figure 2.2: Band structure illustration of bulk and corresponding quantum dot.

also discrete. However, this is just for the case when an electron's confined to an empty sphere. For an actual quantum dot, semiconductor atoms occupy the whole sphere. By using Bloch's periodic wavefunction, effective mass approximation, envelope function approximation and strong confinement approximation, we can get the electron-hole pair states in a quantum dot as

$$E^{QD} = E_g^{bulk} + \frac{\hbar^2}{2a^2}\left(\frac{\alpha_{nh,lh}^2}{m_{eff}^v} + \frac{\alpha_{ne,le}^2}{m_{eff}^c}\right) - E_C \tag{2.4}$$

where E_C is introduced as the Coulomb correction term due to electron hole interaction. For 1s1s transition or the ground electron-hole state, the Coulomb correction is given as $1.786e^2/\epsilon a$ [22]. Clearly with a decreased size, the energy bandgap increases. The discrete band structure of quantum dot is illustrated in Figure 2.2 with $E_g(QD) > E_g(bulk)$. There are a lot of early works that reveal the bandgap size-dependence, especially for CdSe quantum dot [23]. Even from Figure 2.1, we can see the different emission wavelengths at different sizes of silicon quantum dots.

Particle-in-a-sphere model is a good start to look at the band structure of a quantum dot, but it's not accurate enough to get a realistic prediction with too much simplification. The $k \cdot p$ method or the Kane model[25], which looks into higher order terms in $k \cdot p$ method, are typically used to study the quantum dot.

2.1.3 Optoelectronic Properties

Optical transition probabilities in quantum dot are given by Fermi's golden rule

$$P \propto \frac{2\pi}{\hbar} |\langle \psi_f | \hat{H}_I | \psi_i \rangle|^2 \delta(E_i - E_f), \tag{2.5}$$

where $\hat{H}_I = -\hat{\epsilon} \cdot \vec{E}(t)$ is the interaction Hamiltonian in a light field $\vec{E}(t)$ under dipole approximation and $\hat{\epsilon}$ is the polarization vector. The optical dipole moment of quantum dot could be orders of magnitude larger than the bulk materials and thus greatly enhancing the radiative transition rate. We can also look at the problem qualitatively.

Strong spatial confinement increased the Coulomb interactions between electron and hole pairs significantly due to wave function overlapping. This increased the radiative transition rates [24] and thus QDs have higher optical yield than their bulk counterparts. The exciton binding energy is also increased at a smaller size [3, 25], so that the excitons are less subject to thermal perturbation before being extracted out. This helps with the optoelectronic applications.

The density of states (DOS) of a QD also affects the electron relaxation and it can be written as

$$g(E)_{QD} = 2\delta(E - E_c), \tag{2.6}$$

where E is the given energy of where the DOS is calculated and E_c is the discrete conduction band energy level. The delta function comes from the confinement in momentum space k. Clearly with quantized band, the DOS in a QD is also quantized, as shown in Figure 2.3. For a bulk semiconductor, electrons that are known to have very fast thermalization behavior when excited to a high energy level in the conduction band due to continuous band. However, it's more difficult in a system with discrete DOS. A phonon has an energy of multiples of kT(25.7meV at room temperature), which is actually quantized just like photon. While it's easy to match that energy in a continuous band structure, it's much more difficult when it comes to a discrete system. Especially for QDs, the energy difference between first and second excited states could be on the scale of hundreds of meVs. Thus the lifetime for nonradiative relaxation is much longer.

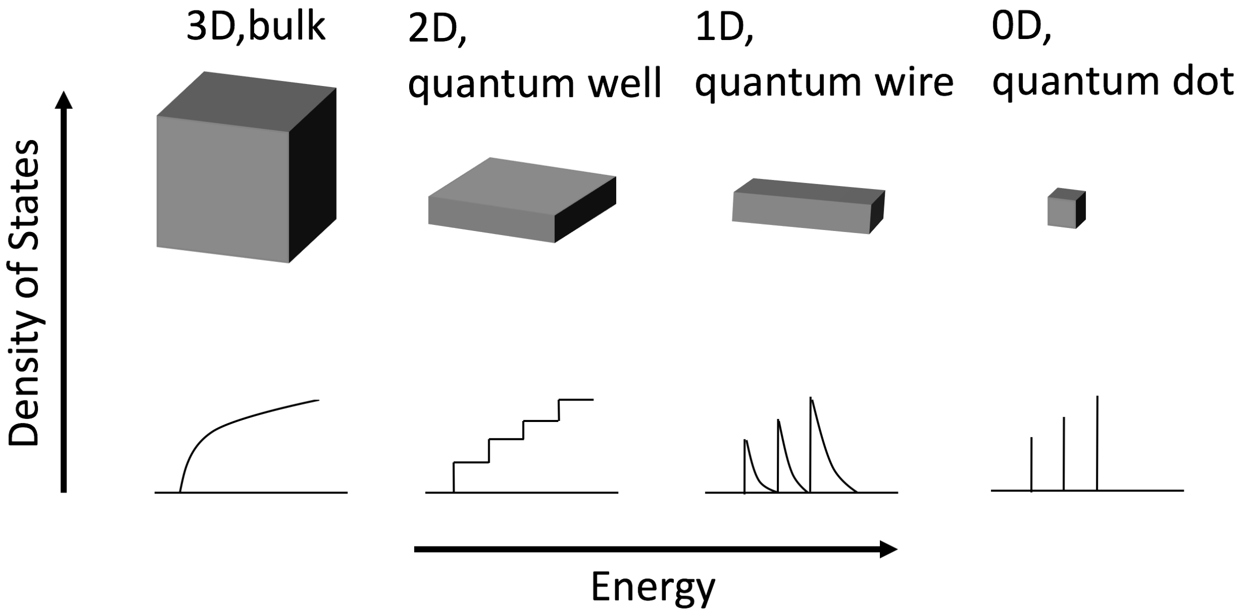

Figure 2.3: Density of states in one band of the semiconductor as a function of dimension.

2.1.4 Synthesis

One of the advantages for CQD is that it can be synthesized through relatively low-cost wet-chemistry methods and form a colloidal distribution of the material, and that's where the word colloidal comes from. La Mer and Dinegar [26, 27] introduced a model to describe crystal nucleation and growth in supersaturated solution. A quick injection of precursor into hot coordinating solvents is applied to achieve supersaturation of monomers in the solution and trigger the nucleation. After the solution concentration falls below the nucleation threshold, no new monomers are formed and the original monomers act as the attracting centers to form bigger crystals. The depletion of the monomers is followed by a slow crystal growth process known as Ostwald Ripening. The average size of the nanocrystals increase overtime but also decreased the overall nanocrystal quantity due to agglomeration of monomers/smaller nanocrystals. The resulting size of the nanocrystal depends on the length of synthesis and solution concentration. Ostwald Ripening greatly facilitates the preparation of a size series of nanocrystals.

2.2 Cellulose Structure

2.2.1 Introduction

Cellulose is the most abundant polymer on Earth and can be found in various of plants such as cotton, wood, and reed, etc., and some animals. It's also one of the materials we use most in our daily life, as can be found in paper and cloth. Being a relatively old material, the development of nanotechnology has rediscovered cellulose for its advantages in abundancy, flexibility and high mechanical strength/weight performance. Cellulose is a has a chemical structure shown in Figure 2.4. It's a member of polyssaccharides consisting of D-glucose units and has a formula $(C_6H_{10}O_5)_n$.

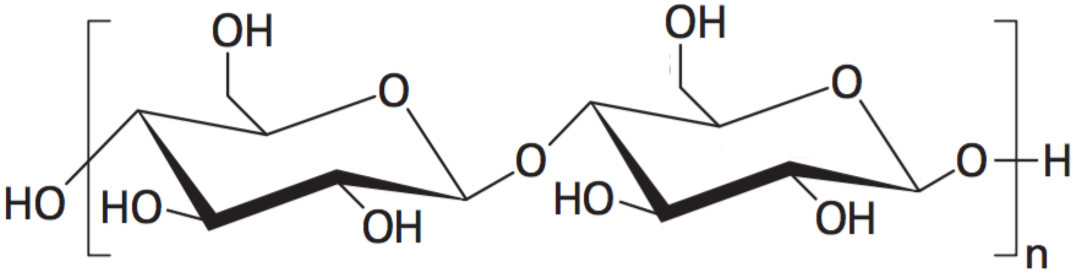

Figure 2.4: Basic chemical structure of cellulose

Wood has 40-50% cellulose that is produced through photosynthesis. It has hierarchical structures that are enforced by semicrystalline cellulose microfibril but also have other elements such as hemicellulose, lignin, waxes and trace elements. Hemicellulose has similar chemical structure as cellulose but has many sugar units. The plant cell wall is supported by all these materials combined to form a framework. Wood contains structures with length scales from meters to nanometers, from the actual tree to cellulose element and is a composite of different materials [28].

2.2.2 Nanofibrillated Cellulose/Nanocellulose

Most of the papers we use in our daily life are formed by cellulose fibers that have a diameter of tens of micrometers. These cellulose fibers are actually consist of thousands of microfibrils with diameter of tens of nanometers. The microfibrils are made of much smaller primitive cellulose units as the cellulose nanocrystals, which has much higher crystallinity. Nanofibrillated cellulose(NFC) [29] or nanocellulose is close to microfibrils and is a name used more for nanotechnology. While normal papers are rough, opague and porous, by decreasing the dimensions of cellulose units, we can get much more transparent, smoother and stronger papers. However, papers made of cellulose nanocrystals are not as flexible as NFC ones due to higher crystallinity, but they have very good mechanical strength.

We can nanofibrillate larger cellulose fibers through strong mechanical disintegration process, such as high-pressure homogenization/microfluidizing, grinding, cryocrushing, and high-intensity ultrasonication. However, these processes require a lot of energy consumption and the flocculating nature of the fibers can damage the narrow slit in a microfluidizer [30]. Thus it's not economic for mass production by bare mechanical disintegration processes. A lot of pretreatment methods are introduced to degrade the mechanical structure of the fibers before mechanical treatment, such as Enzymatic pretreatment, carboxymethylation and 2,2,6,6-tetrameth-ylpiperidine-1-oxyl(TEMPO)-mediated oxidation [31, 32]. Among them, TEMPO-mediated oxidation is most commonly used to convert the regenerated cellulose into polygucuronic acid, which is water-soluble. But it only oxidize the surfaces of microfibrils and thus maintain the fibrous nature of the cellulose fiber. It also introduces anionic carboxylate groups to the celluloses and the resulting electrostatic repulsion between TEMPO-oxided celluloses overcome the interfibrillar hydrogen bonds present in the cell walls. This helps the distribution of the cellulose in water and makes it easier for further mechanical treatment.

2.2.3 Mechanical, Thermal and Optical Properties of NFC

The mechanical properties are of great interest in the study of cellulose, since being offered by our Mother Nature, it's original function is to reinforce cell walls in plants. Numerical studies found that nanocellulose has a Young's modulus in the range of 100-130Gpa, which is much higher than glass fiber and potentially close to stainless steel [33]. Nanopapers made of nanocelluloses have a Young's modulus of 7-14GPa [34,35], which is still significantly higher than normal papers, which has <1 GPa modulus.

Cellulose nanocrystals has a low coefficient of thermal expansion(CTE), which is estimated to be 0.1 ppm K^{-1}. But for the nanofibrillated cellulose we are gonna use, the value can vary from 12-30 ppm K^{-1}, but it's still significantly smaller than most of the polymers [35]. Nanocellulose also has a relatively high thermal stability with no chemical degradation or decomposition to 200-300°C.

Optical properties have also been studied for nanocelluloses. With the size to be in 10s of nanometers, which is far smaller than the wavelengths of visible light, nanocellulose films have good optical transmittance compare to polymer and microcellulose films(paper). Though further optical engineering, the transparency can surpass 90%. We are also gonna demonstrate ultrathin NFC membranes with a transparency over 97%.

In view of its mechanical strength, thermal stability and optical properties, nanocellulose is an ideal material for optoelectronic applications.

2.2.4 Optoelectronic/electrical Applications

Being an old and cheap material, people have long used paper as dielectric layer for energy storage devices [36, 37], field effect transistors(FETs) [38, 39], and as substrate for LEDs [40] and other devices [5]. However, the high roughness and the porous structure of the microfiber-based paper deteriorate the performance of these devices significantly. Ref [41] compared FETs fabricated on both paper and plastic substrates. Even though similar device structure and materials are used for fabricating FETs, the device on paper shows more than tens times lower current at the same voltage and larger hysteresis when compared with the plastic substrate.

The discovery of nanocellulose-based papers solved a lot of problems. As mentioned in previous sections, nanocellulose has superb optical, mechanical and thermal properties that are much better than other polymers. This makes it ideal substrate material for a lot of applications. Its fiberous nature also opens up room for different functionalities with other materials. High performance conductive papers are fabricated with the incorporation of nanomaterials such as Ag nanowires [42, 43] and carbon nanotubes [44]. Metal and semiconductor nanoparticles are also added to make optical sensing platforms [45], magnetic papers [46,47] as well as photoluminescent papers [48]. It can also go through optical engineering for higher haze [49] or transparency [50] for different applications. Thus nanocellulose is very promising for flexible devices.

2.3 Photodetection Mechanisms

Semiconductor photodetection is about detecting photons from light(visible, ultraviolet, infrared, X-ray, microwave, etc.) and converting them to electrical signal. When a photon with an energy of which is larger than the bandgap of the semiconductor it illuminates on, it will excite an electron from the valence band to the conduction band and leave a hole in the valence band. Ideally, that electron and the hole are free to move in the semiconductor and can be separated upon the presentation of an electrical field, which can come from an external bias or internal junction.

Although colloidal QD has some diffrerences comparing to its bulk counterpart, they are governed by the same physics when made into devices in a macroscopic scale. Hence it’s helpful to go through basic device structure and carrier transportation mechanisms. Generally, by how the carriers are extracted, photodetectors can be divided into several categories, such as photoconductor and photodiode. A photoconductor is always operating under a flat band condition with both ends interfacing electrodes through Ohmic contact. Thus normally electrons can circulate the whole detection system multiple times and result in high gains. A photodiode has a depleted region in the junction area where two material contacts. High electric field is present in this region and quickly separates free carriers to create current. Thus usually diode has much faster response speed. There are several kinds of photodiode, p-n junction diode, p-i-n junction diode, Schottky junction diode,

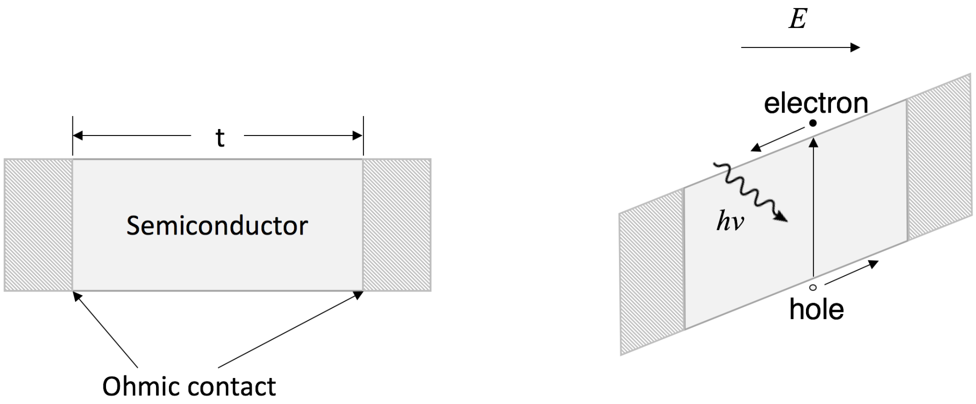

Figure 2.5: A schematic of photoconductor structure and when under bias.

etc. There is also a special kind of diode that uses avalanche effect to greatly improve the device response when the device is operated under a very large reverse bias.

2.3.1 Photoconductor

A photoconductor is a very simple device with the semiconductor being interfaced by two Ohmic contacts at both ends, as is shown in Figure 2.5. When free carriers are generated, they will be driven by the external field and create current. In an electrical engineering view, more free carriers mean more conductive and less resistive. The conductivity of a photoconductor σ can be written as

$$\sigma = q_e(\mu_n n + \mu_p p), \tag{2.7}$$

where q_e is the charge of an electron, n and p are electron and hole concentrations, μ_n and μ_p are mobilities for electrons and holes, respectively. n and p are always equal if there's no other effects such as carrier trapping and should be equal to the number of photons absorbed. However, in a real device, a lot of reflections and scatterings do occur during illumination and multiple phonon involved processes could decrease the number of carriers generated. It's safe to introduce a parameter η, namely quantum efficiency and is defined as:

$$\eta = \frac{\#_{electron}}{\#_{photon}}, \tag{2.8}$$

Quantum efficiency defines the efficiency of electron generation by a single photon illumination and is usually smaller than 1 due to processes mentioned above, however in quantum dots, it's possible that multiple electrons are excited upon absorbing one photon. That is due to much larger Coulomb interaction in a confined region and large exciton binding energy. Therefore it's possible that quantum efficiency is larger than unitary. For simplicity, we can ignore multiexciton process and write out the electron/hole concentration in steady-state generation as

$$n = p = \eta \frac{P/A}{h\nu} \frac{\tau}{t}, \tag{2.9}$$

where P is the absorbed optical power in an area of A, τ is the carrier recombination time and t is the thickness along the external electric field E. From Ohm's law, we have the photocurrent as

$$I_p = J \cdot A = \sigma E \cdot A = q_e \eta \frac{P}{h\nu} \frac{(\mu_n + \mu_p)E}{t} \tau, \tag{2.10}$$

$E = V/t$, where V is the applied bias. In a quantum dot system, due to surface states, a lot of times either hole or electron is trapped, thus we can simplify the mobility to only one kind of carriers as μ. By simplifying and rearranging equation 2.10, we have

$$I_p = q_e \eta \frac{P}{h\nu} \frac{\mu E}{t} \tau = q_e (\eta \frac{P}{h\nu}) \frac{\tau}{T_{tr}} = q_e N \cdot \Gamma_G, \tag{2.11}$$

where N is the electron/hole generated under certain illumination power, Γ_G is the photoconductive gain due to the circulation of carriers in the circuit before recombination.

2.3.2 Schottky Junction

Schottky diode is one kind of photodiode that has a depletion region at the metal semiconductor interface. When an n-type semiconductor contacts with a high work function metal, in order to align the Fermi level, electrons are depleted from the semiconductor side(Figure 2.6a). Thus bends the semiconductor band structure and creates a barrier at the interface. The barrier height is given as

$$\phi_{SB} = \phi_M - \chi, \tag{2.12}$$

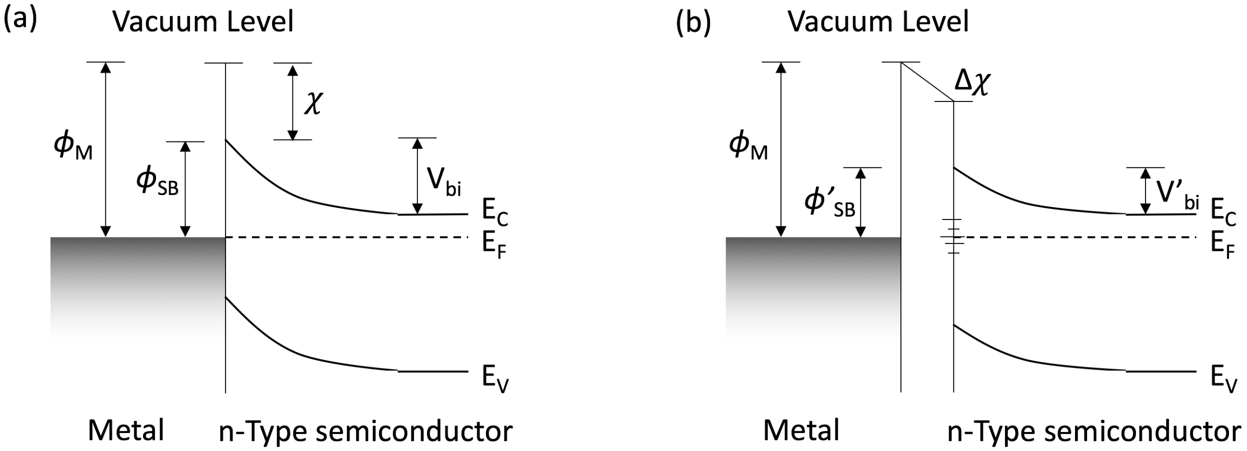

Figure 2.6: Energy band diagrams of metal-semiconductor interface without(a) and with(b) interface states.

where ϕ_M is the work function of metal and χ_{SC} is the electron affinity energy of the semiconductor, which is the energy difference between the bottom of the conduction band to the vacuum level. However, due to surface oxidation, surface contamination or simply diffusion between metal and semiconductor, interface states could be created between metal and semiconductor interface, thus altering the barrier from the ideal case given by equation 2.12, as shown in Figure 2.6b. The barrier could be already set before the contact between semiconductor and metal, and this is called Fermi level pinning. The resulting barrier height can be written as

$$\phi_{SB} = \phi_M - \chi - \Delta\chi, \tag{2.13}$$

where $\Delta\chi$ is the potential across the interface state. For materials like colloidal quantum dots, they always have some surface states due to abrupt stop in lattice growth on the surface, especially the ones without surface passivation. Therefore the contact between high work function metals and CQDs may not be ideal Schottky junction.

The carrier transport in a Schottky junction can undergo different mechanisms, such as thermionic emission, tunneling, recombination, etc. Under most cases, thermionic emission is dominant. Thermionic electrons are the electrons that have a thermal energy larger than the barrier so that they can freely move from semiconductor side to the metal side. With a forward bias voltage V, the thermal equilibrium will be broken and the electron potential will be changed by qV. The electron density that is over the barrier can be computed by looking into the Fermi-Dirac distribution and DOS of the electron under certain potential. I am not going to give out all the details here but the resulting current due to thermionic emission is given as

$$I = A^{*}T^{2}\exp(-\frac{q\phi_{SB}}{kT})[\exp(\frac{qV}{kT}) - 1], \tag{2.14}$$

where A^{*} is the Richardson constant, kT is the unitary thermal energy with k the Boltzmann constant. We can also write the Richardson constant as

$$A^{*} = \frac{4\pi m^{*}k^{2}q_{e}}{h^{3}}, \tag{2.15}$$

with m^{*} the electron effective mass and h the Planck constant.

The photoconduction in Schottky junction can have different mechanisms depending on the absorbed photon energy $h\nu$.

1. When $h\nu$ is larger than the barrier height ϕ_{SB} but smaller than the semiconductor bandgap E_g, that will excite some electrons in the conduction band to a level that surpasses the barrier and thus results in current due to the build-in electrical field at the junction.

2. When $E_g < h\nu < E_g + \phi_{SB}$, the valence band electrons are excited to the conduction band but the energy is not high enough to surpass the barrier. The electrons will still populate the conduction band but the current could be limited by the unmatched thermal energy.

3. When $h\nu > E_g + \phi_{SB}$, valence band electrons are excited a level that goes over the barrier, this will result in maximum current.

Chapter 3

CDSE QD PHOTOCONDUCTOR WITH INK-JET PRINTED ELECTRODES

In this chapter, flexible photodetectors fabricated on transparency films and tracing papers are reported. PEDOT:PSS (poly (3,4-ethylenedioxythiophene) : poly (styrenesulfonate)) has long been reported as a material for transparent electrodes with high conductance, high transparency, thermal and electrochemical stability [51]. PEDOT acts as the main conductive part, while PSS is the water-soluble polyelectrolyte to provide this material with solution-processability. Though ITO (indium tin oxide) has better performance in conductance and is still widely used in today's transparent optoelectronic devices, its flexibility [52] is limited and the cost remains high due to the inclusion of rare earth material indium and vacuum deposition method. PEDOT:PSS is promising in a way that it can be deposited and patterned easily with state-of-the-art printing techniques with decent performance and low cost.

Inkjet printing method has been exploited by many researchers to deposit solution-processable materials such as conductive polymers [53,54], quantum dots [55], metal nanoparticles [56], carbon nanotubes [57], etc. Comparing with other fabrication methods such as spin-coating and thermal evaporation, inkjet printing offers a way to significantly lower the cost and material wastage while at the same time being able to deliver large-area and mask-less noncontact precise patterning at a high speed. While precise control of each droplet can be achieved with a complicated material printer like Dimatix DMP-2800, commercially available low-cost office inkjet printers [58] have been proved to be reliable for patterning well-controlled PEDOT:PSS films with little system modification. Moreover, the commonly used image processing software like Adobe Photoshop has the ability to precisely control printing patterns to a single pixel, which further facilitates the exploitation of office inkjet printer for material thin-film printing.

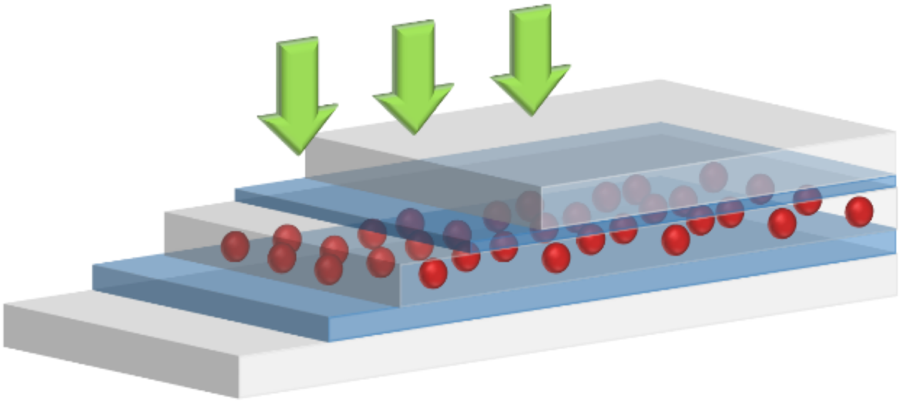

Figure 3.1: Schematics of a flexible NCQD photoconductive detector. Materials for layers from top to bottom: transparency film/PEDOT:PSS/tracing paper (CdSe QDs)/PEDOT:PSS/ transparency film. Light illumination is from the top.

In terms of flexible substrate materials, polyethylene terephthalate (PET) substrates serve well for ink-jet printing purpose. The transparency film, commonly used for classroom presentations, is one of the most available and cost-efficient materials among all kinds of PETs. Its transparency, mechanic and electrochemical durability, as well as high smoothness make it an ideal substrate for low-cost flexible optoelectronic devices.

3.1 Device Design

The device structure is shown in Figure 3.1. It consists of a CdSe QD embedded tracing paper layer and two inkjet printed PEDOT:PSS layers on transparency films to form a photoconductor structure.

While it's convenient to use unmodified transparency film and inkjet printing for polymer electrodes deposition, the large surface roughness should be taken into account, which makes it hard to deposit smooth active layers on top and the device could easily be short-circuited if the active layer is thin ($<1\ \mu$m). Tracing paper is introduced as the interspacing layer for active material embedment and withal to prevent short-circuiting. The porous cellulose structure helps with the adhesion of CdSe QDs and also makes the device fabrication to be much more obvious and simpler.

3.2 Device Fabrication

3.2.1 Inkjet printing with office printer

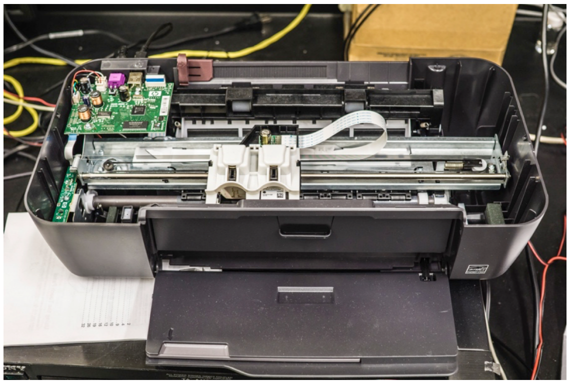

Figure 3.2: The desktop inkjet printer used for PEDOT:PSS deposition

PEDOT:PSS electrodes are printed with an HP1000 thermal office inkjet printer (Figure 3.2) on an unmodified letter-size transparency film (PP2500 from 3M). Original HP61 black cartridge, which is compatible with the printer, is cleaned and without further modification. Patterns are precisely controlled with accuracy to a single pixel by Adobe Photoshop. Unlike the film thickness control method described in reference[30], we set the luminosity to be zero, i.e. the color seen on the computer screen is totally black, to obtain highest thickness and thus the best conductance. PEDOT:PSS ink (Sigma-Aldrich), 0.8% solids in water, is prepared with 0.1% (vol.) Triton-X 100 as surfactant to prevent formation of “coffee rings”during printing and achieve good film uniformity. The formulation is injected into the cartridge with a syringe through a 0.45μm filter to filter out large particles to prevent nozzle clogging. Multi-layer printing is achieved simply by adding the printed films back to the printer paper holder and align with the edge of the paper holder, then repeat the printing process. The electrodes are baked under 80-100°C in ambient atmosphere for about 10 minutes to dry the solvents after each printing to avoid the damage that can be caused by the rolling system of the printer during next printing. Sub-100μm alignment accuracy is achieved for multi-layer printing along the rolling direction. We discovered that slight

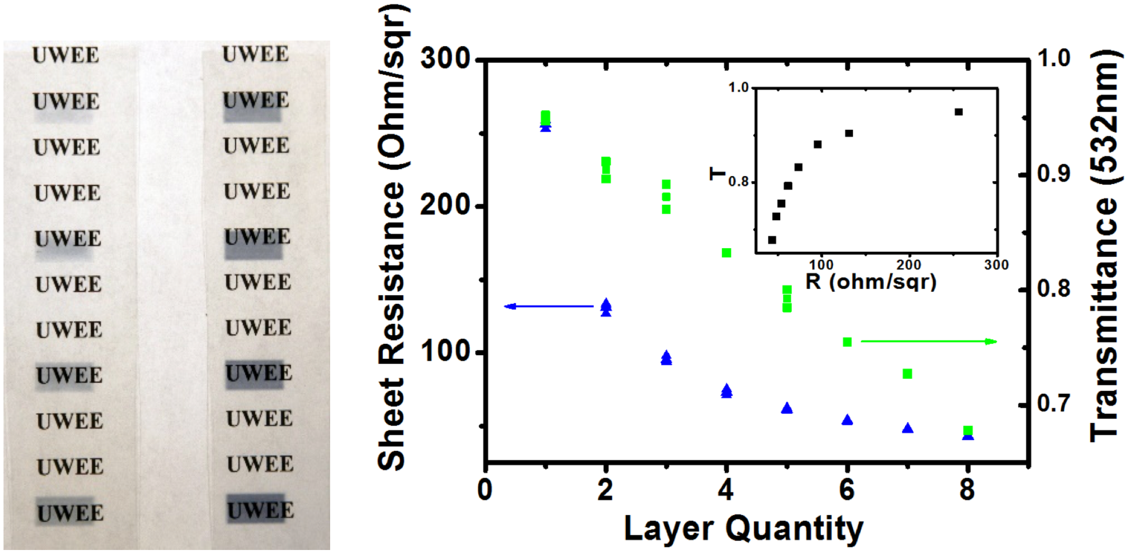

(a) (b)

Figure 3.3: (a)A photo of the electrodes with different number of layers on a white paper with texts; Layer quantities from top left to bottom left is 1 to 4, and 5 to 8 for top right to bottom right. (b)Sheet resistance and transmittance for inkjet-printed PEDOT:PSS films as a function of the layer quantity. Multiple measurements were taken at different regions. Inset: transmittance vs. sheet resistance.

misalignment in each printing actually helps to smoothen the film and improve conductivity due to the non-even polymer distribution in the formulation. After the whole printing cycle, the electrodes are annealed at the same temperature mentioned above for 2 hours or more to dry all the organic and water residues.

Uniform polymer electrodes with areas of 5 mm × 10 mm were printed with variation in layer quantities from 1 to 8 (Figure 3.3a). The transmittance of the printed film decreases when the layer number increases, which is seen visually. The sheet resistance was measured by four-point probe technique and the results are shown with film transmittance under 532 nm light illumination in Figure 3.3b. Note that the transparency film itself contributes to 10% light loss (as can be seen visually in Figure 3.3a, comparing to the center part of the paper without the transparency film) and the data shown in Figure 3.3b is the net transmittance for the PEDOT:PSS film. Linear dependence of transmittance on layer number is obtained, while for resistance the value decreases hyperbolically with the layer number. It is because the multi-layer electrodes act as parallel resistors due to the baking after each printing.

The relation between film sheet resistance R_{sh} and transmittance T is given by the following equation [59]:

$$T = (1 + \frac{Z_0}{2R_{sh}} \frac{\delta_{op}}{\delta_{dc}})^{-2}, \tag{3.1}$$

where Z_0 is the impedance of free space (377Ω), δ_{op} and δ_{dc} are the optical and electrical conductivities, respectively. The value δ_{op}/δ_{dc} is normally used to evaluate the performance of transparent electrodes, and traditional metal oxide electrodes have $\delta_{op}/\delta_{dc} \sim$ 35. It's always important to have high transmittance and low sheet resistance, and thus it's better to have large δ_{op}/δ_{dc} value. For our PEDOT:PSS electrodes, the value obtained is $\sim$28, which is slightly smaller than the metal oxide electrodes but acceptable. As shown in Figure 3.3b, sub-100Ω/□ sheet resistance is obtained with $>$85$\%$ transmittance with 3 layers of printed PEDOT:PSS. The result shows the feasibility of using inkjet-printed PEDOT:PSS electrodes for flexible optoelectronic devices.

In terms of device fabrication, it is very important to balance the transmittance and resistance of the electrodes. For the bottom electrodes, we simply use the 8-layer films since there's no light illumination from the bottom and the resistance should be as low as possible to achieve efficient carrier transport. For the top layer where the optical transparency is important, we should consider the photoconductivity equation. According to Ref.[65], we can write the photocurrent I_p under bias voltage V and optical illumination power P_{opt} as:

$$I_p = q\eta \frac{P_{opt}}{h\nu} \frac{(\mu_n + \mu_p)\tau}{t^2} T(V - I_p R), \tag{3.2}$$

μ_n and μ_p are electron and hole mobility in quantum dot, respectively. $h\nu$ is the illumination photon energy and q is the electron charge. τ is the carrier lifetime. t is the thickness of the NCQD thin film, and here it is roughly the thickness of the tracing paper but could be changed when compressing the structure. η is the quantum efficiency of the NCQD thin film. R and T are the resistance and transmittance of the electrodes. We can solve the equation iteratively, or as a good approximation, we can ignore the voltage drop through the electrode, because of the relatively

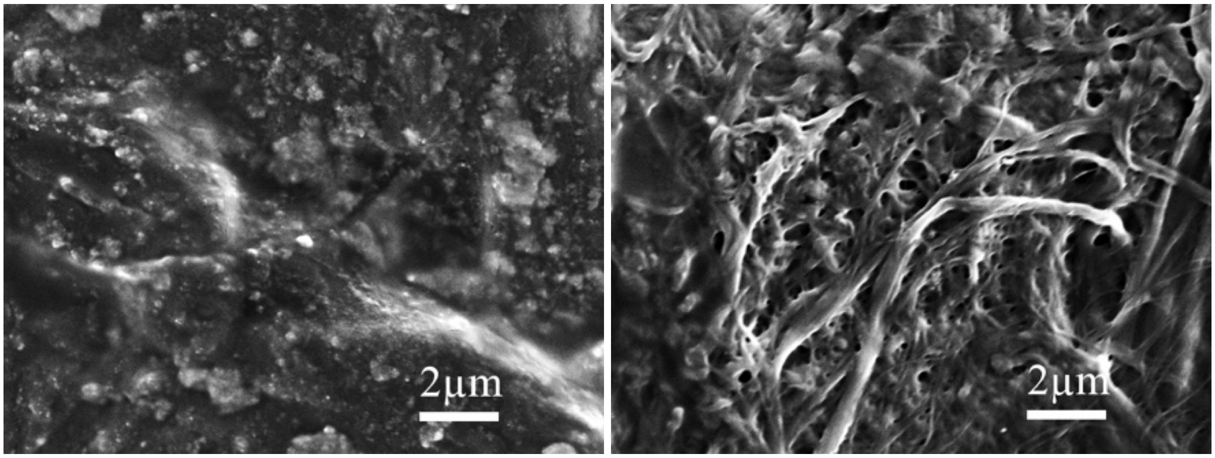

(a) (b)

Figure 3.4: SEM image of the fiber cellulose structure of tracing paper with (a) and without (b) CdSe QDs.

good conductance of the electrodes ($< 150\Omega/\square$ for two or more layers) compared to the NCQD thin film ($\sim$MΩ). Therefore, a linear dependence of the photocurrent on the light transmittance is a good approximation. In consideration of film uniformity, electrical conductance and optical transparency, we choose 3-layer PEDOT:PSS as the top electrodes.

3.2.2 QD preparation and Device integration

CdSe quantum dot (NN-LABS, Emission Peak at 630nm, 5.2-6.2nm in size, suspended in toluene, -Octadecylamine), is used in the photodetector acting as the photoconductive semiconductor material. In order to reduce the influence of ligands on photoconductivity, we washed the original NCQDs at least 3 times in toluene and ethanol mixture before deposition. Each wash is done with ethanol and subsequent centrifuging. The precipitations are redissolved by toluene for next wash or deposition. The prepared QDs are drop-casted onto as-purchased tracing paper (Roselle Paper, $\sim$35μm thick) instead of being coated on the electrodes directly. The optical transparency at 532nm for the tracing paper used in the experiments is $\sim$25%. However, strong light scattering effect in the fibrous structure helps to enhance the light absorption of QDs. To maximize the QD

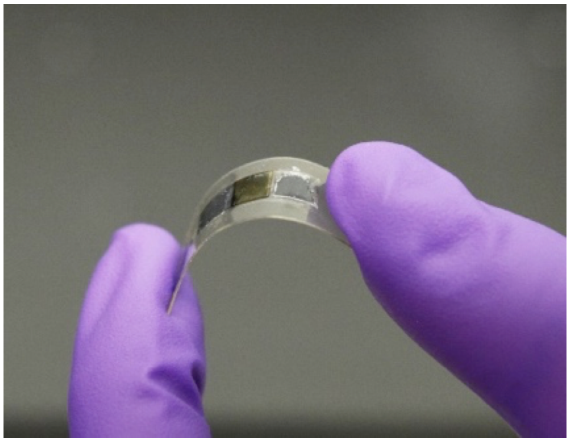

Figure 3.5: A photo of the flexible photoconductor under bending

density in the tracing paper to increase photoresponsivity of the device, multiple drops of QDs are deposited until sufficient density is obtained. SEM images for tracing paper cellulose structures with and without QDs are shown in Figure 3.4a and 3.4b. QDs are attached to the fibers and form continuous films along the fibers. The QD-soaked tracing paper is sandwiched between two PEDOT:PSS electrodes printed on transparencies after solution being dried and the device is laminated with glue. While it's not straightforward to obtain glue with both good conductivity and transparency to laminate the active layer, we apply glue at the periphery of the tracing paper on transparency films. Two flat metal plates are used to clamp the device until the glue's dried. An actual flexible device is shown in Figure 3.5.

3.3 Measurement Results and Discussion

3.3.1 I-V response and bending test

The photodetector is characterized using a Cascade M150 low-noise probe station and a 532 nm continuous laser source with an intensity of 75 mW/cm^2 at a spot diameter of 2.44mm. About 75 μg CdSe NCQDs are dispersed in the tracing paper and resulting in a density of $\sim$75 mg/cm^3. In this work, we characterized the device performance under bending radii of 4.8 mm, 5.5 mm, 6.5 mm, and 9.2 mm (Figure 3.6). With a decrease in bending radius, we find the response of the

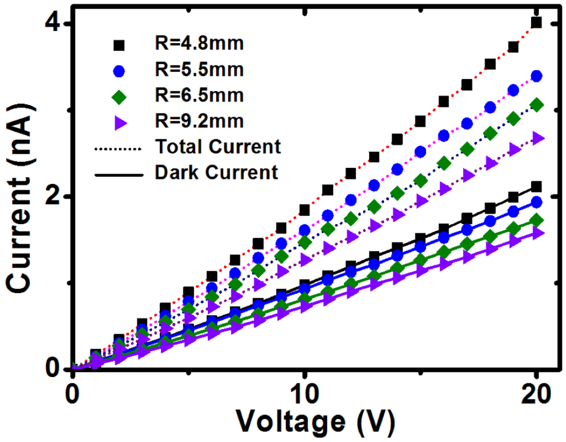

Figure 3.6: I-V characterizations of the device with bending radii of 4.8 mm, 5.5 mm, 6.5 mm, and 9.2 mm, under 532 nm light illumination.

device increase both in dark current and total current under illumination. We attribute the reason to that the bottom transparency film tends to have a smaller radius than that of the top film under bending, which squeezes the cellulose tracing paper. Hence the device with smaller bending radius tends to have thinner interlayer spacing. In view of the insulating nature of tracing paper, the conductivity of the NCQD film is mainly from the tunneling between the nano-particles, as typical NCQD devices. Therefore thinner spacing leads to better photoconductivity, as is also shown in Equation 3.2. The fluctuation in the curve is mainly due to the unstable laser source. The relatively low response of the current device is due to the large interlayer spacing and scarce NCQD density in cellulose structure.

In order to improve the performance, an easy way is to clip the device between two stiff plates, which could be under bending, and we were able to obtain significantly better results using this approach [60]. An alternate way is to use a thinner and more porous material as interspacing layer We found bio-membranes, such as tree leaf, reed inner membrane, etc., have much thinner and more porous structures as well as better transparency. Higher photoresponsivity (>1% EQE) has been found by applying these membranes in substitution of the tracing paper. More experiments and investigation are currently underway.

For applications in wearable flexible devices, the device should maintain its performance after many times of bending. We have performed this test on our flexible NCQD photodetector and found our device is able to maintain consistent performance after more than 100 times of bending. In terms of long-term reliability, we have seen little degradation in the performance of our devices after 2 months storage time. The sandwich structure helps to protect the device from degrading without further encapsulation process.

3.3.2 Saturation test

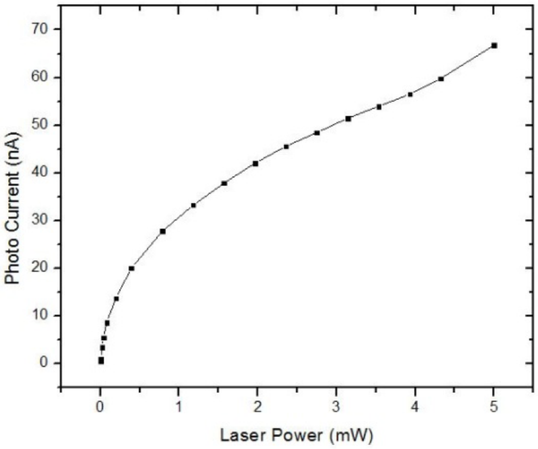

Figure 3.7: Photocurrents versus laser power under 30V bias.

The saturation test was performed with a device with the same structure but clamped between two glass slides to form better contact and thus it has much higher performance than the one shown in section 3.3.1. The result is shown in Figure 3.7. The device tends to saturate when the laser power goes high.

Chapter 4

FLEXIBLE ZNO QUANTUM DOT UV PHOTODETECTOR ON BIO-CELLULOSE STRUCTURE

Ultraviolet (UV) detection has been extensively studied thanks to its wide applications in communication, pollution monitoring and medicine. While high performance UV photodetection has been achieved even for commercial use, the rigidity of these devices limits their usage for applications requiring portability and wearability, which is the current trend for commercial electronics. This is where solution-processable nanomaterials can make distinguishable contributions. Low-cost flexible devices have been made possible by utilizing materials such as quantum dot (QD) quantum dots and nanorods. Wet-chemistry synthesis [61–63] of these materials not only helps reducing the material cost, but also offers solution-processability, which enables low-cost, facile and large-scale fabrication. In addition, the 3D-confinement of electrons in QDs leads to high quantum efficiency and a tunable bandgap depending on the particle size [64, 65], and thus offering the convenience of tuning the absorption spectrum edge for different optoelectronic applications. In terms of UV detection, ZnO QD is a very promising material for flexible devices. With a bulk bandgap of 3.37eV, ZnO has excellent absorption in UV and remains transparent to visible light, i.e., it's a naturally visible-blind material.

In this chapter, UV photodetectors are fabricated, as far as we know, for the first time on a reed plant membrane. The material is commercially available as the vibration membrane for Chinese bamboo flutes. At a thickness of $\sim$5 μm when compressed, the membrane is significantly thinner and more porous than most of the commercial papers ($>$30 μm) and thus offers much better transparency.

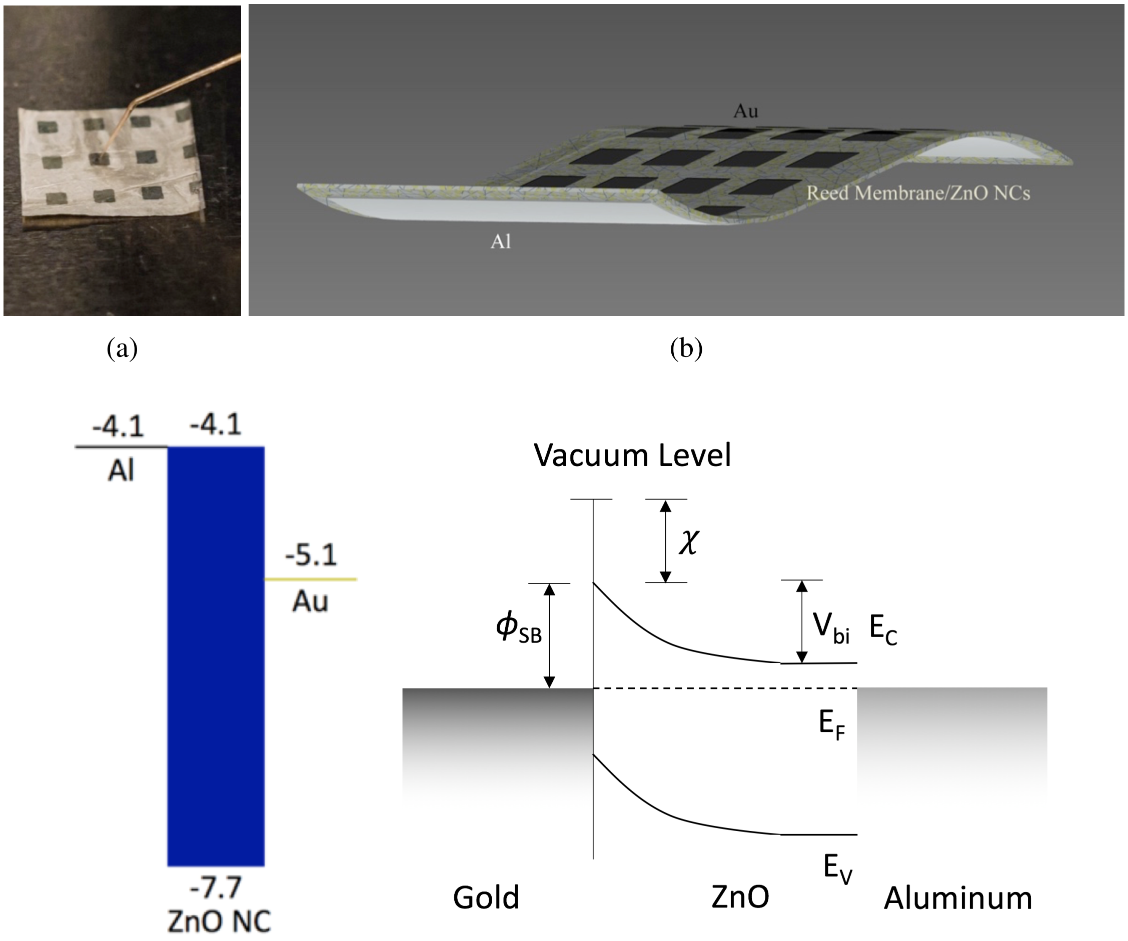

(a) (b)

(c) (d)

Figure 4.1: (a) An array of ZnO UV flexible photodetectors fabricated on a reed membrane. The photograph shows one of them under test using a probe; (b) Schematics of the device structure; (c) The work function diagram of the device (unit: eV); (d) Band structure of the device after aligning the Fermi level.

4.1 Device Design and Principle

We designed a vertical structure for the device that consists of a ZnO QD-embedded reed membrane sandwiched between gold and aluminum electrodes. The actual devices are shown in Figure 4.1a and the structure is illustrated in Figure 4.1b. Though lateral photoconductor structure is typically of interest due to its simplicity and potentially high optical gain, ZnO QD-based flexible UV photoconductors in general suffer from slow response due to the large number of trapping states and slow carrier mobilities compared to bulk semiconductor material. By using the cellulose structure as an interspacing layer with the active material embedded, a Schottky junction structure can be readily achieved between ZnO and Au as shown in Figure 4.1c and 4.1d, which improves the response speed. While thin-film Au and indium-tin-oxide (ITO) can both serve as transparent electrodes and are of high work functions that can result in Schottky junctions interfacing with ZnO, ITO becomes opaque at UV region and it also has poor flexibility due to the ceramic-like crystal structure. Given these plus further consideration in fabrication simplicity, we chose Au as the transparent electrode for our device despite that ITO is currently the most widely used transparent electrode material. Furthermore, Au also shows good adhesion on the cellulose structure and requires no additional adhesion layer, which further simplifies the deposition process and increases the transparency and conductivity of the device as well. An Ohmic contact is formed between Al and ZnO (Figure 4.1c and 4.1d). With such a device design we are able to operate the device without external bias, i.e. the device can be operated with photovoltaic effect and is therefore self-powered.

4.2 ZnO QD Synthesis and Test

4.2.1 ZnO QD Synthesis

ZnO QDs are synthesized using well-developed wet-chemistry method, as is shown in Figure 4.2. 2.92g Zinc acetate dihydrate is dissolved in 125ml methanol. 1.48g Potassium hydroxide is dissolved in 65ml methanol upon sonication and then mixed with $Zn(Ac)_2{\cdot}2H_2O$ solutions drop-wise at ∼65°C. The reaction then takes two and a half hours with the solution turning turbid and fol-

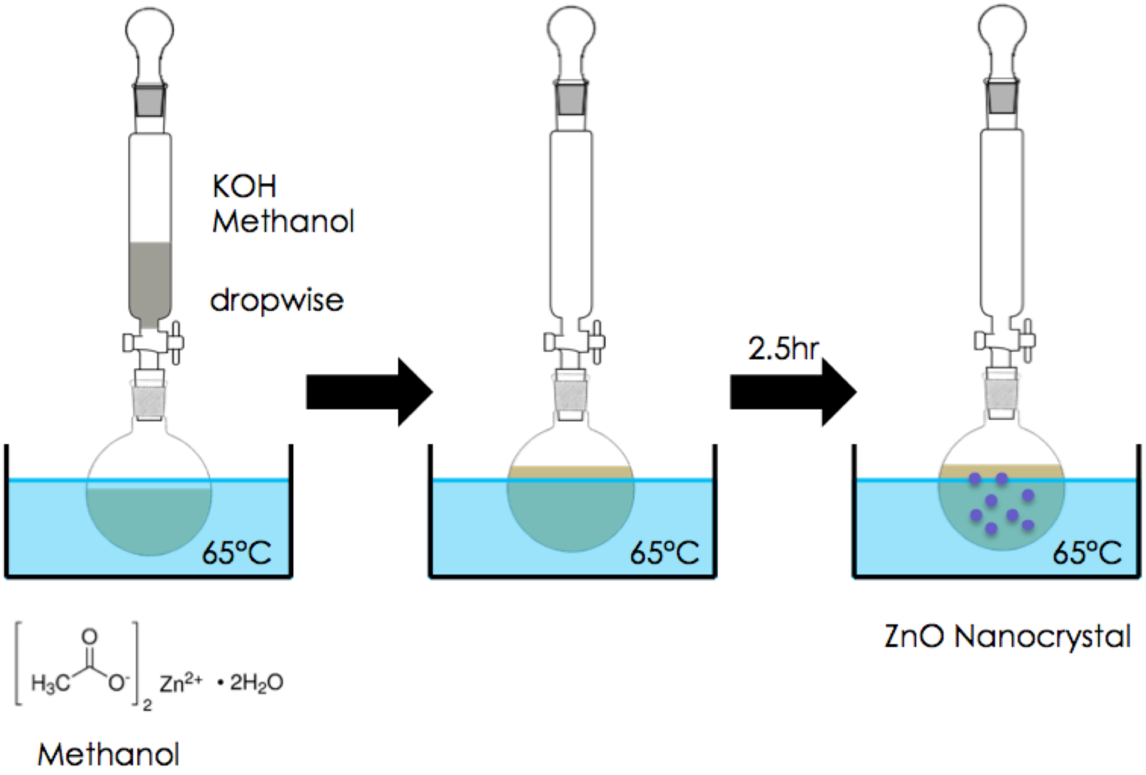

Figure 4.2: ZnO quantum dot synthesis process

lowed by centrifug∼ing to precipitate out the QDs. The precipitation is washed in methanol twice with centrifuging and then dissolved in 15ml butanol and 1ml chloroform to form a clear and transparent solution with a ZnO QD concentration of ∼30mg ml^{-1}. A quantum dot size of ∼6nm is achieved through this process. These QDs are air-stable for weeks with magnetic stirring.

4.2.2 Material Characterization

TEM

The TEM images of the ZnO QDs synthesized from the above wet-chemistry method is shown in Figure 4.3. QD sizes of 5-7nm are observed. Clear lattice structures can be seen from the TEM image in Figure 4.3b.

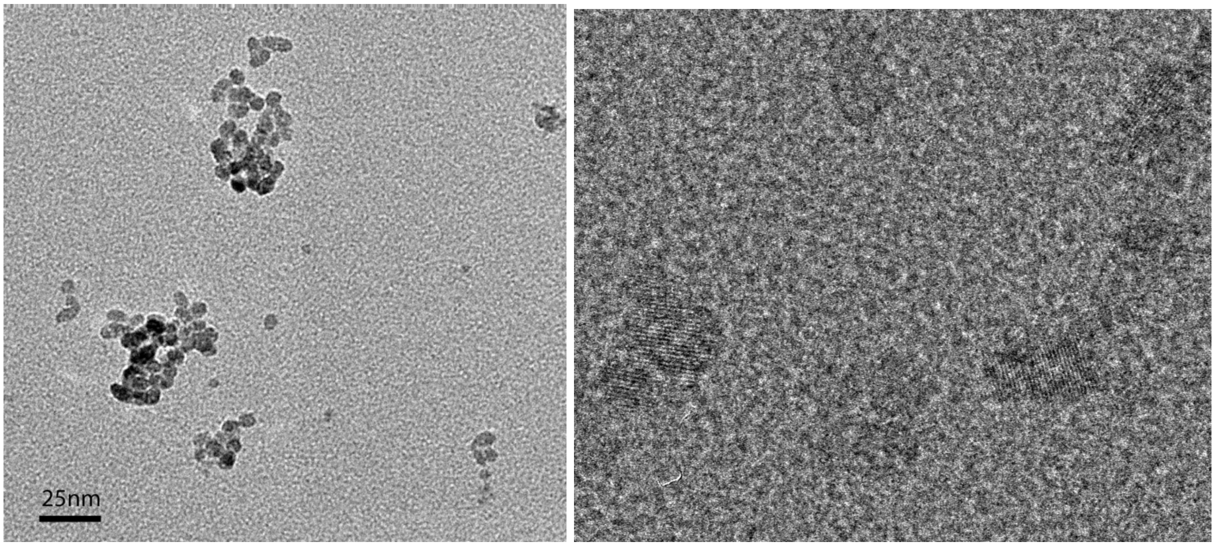

(a) (b)

Figure 4.3: (a) A TEM image of clusters of ZnO QDs; (b) Zoom-in of individual ZnO QDs with clear lattice structures.

UV-vis Absorption

The UV-vis measurements are done with Varian Cary 5000 UV-Vis-NIR spectrometer. The result is shown in Figure 4.4. Absorption starts at $\sim$350nm, which indicates a bandgap of 3.55eV. It's larger than the bulk band gap of ZnO, but is in cope with that of the QDs. No absorption is seen in visible range (the nonzero values at visible range is due to the background absorption).

4.3 Device Fabrication

4.3.1 Device Fabrication Process

The device fabrication process is shown in Figure 4.5. Before depositing ZnO QDs, reed membranes are soaked in KOH overnight and then rinsed in methanol and isopropanol. After that, they are soaked in ZnO QD solution overnight and have the QDs embedded in the cellulose structure. Upon being dried in vacuum, Al films with a thickness of 150 nm are thermally evaporated on one side of these substrates to form common contact, and followed by another thermal evaporation of

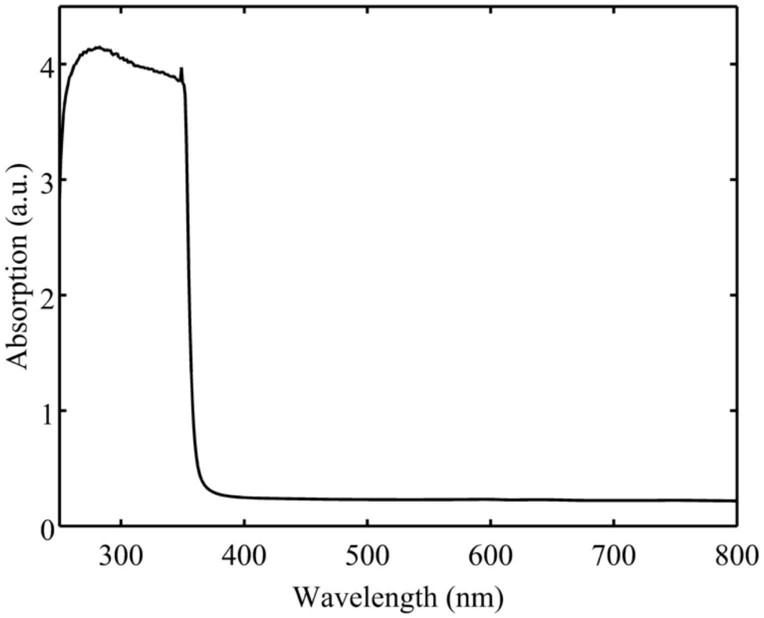

Figure 4.4: UV-vis absorption spectrum of ZnO QD in butanol.

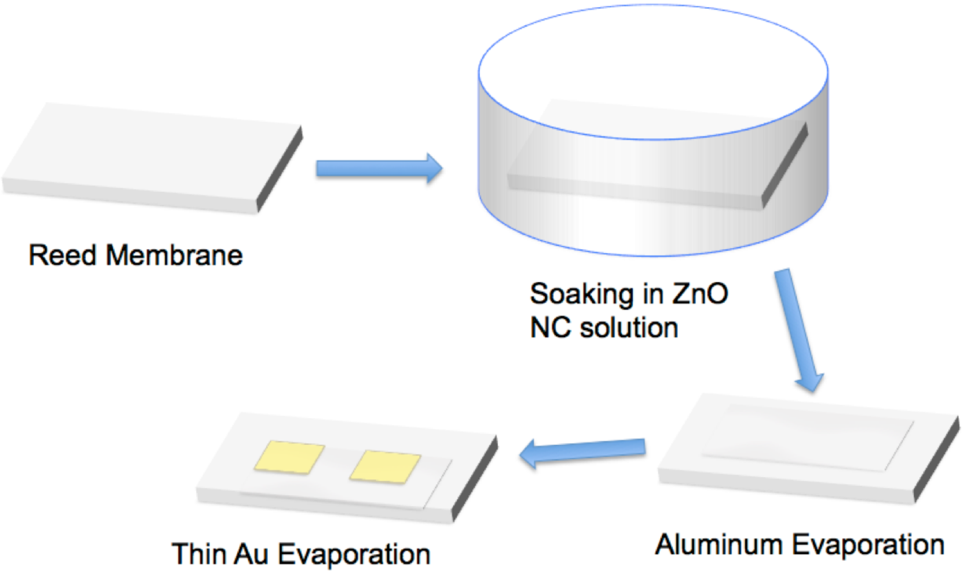

Figure 4.5: Fabrication processes for flexible ZnO quantum dot photodetector on a reed membrane.

25nm-gold-film with features of 1.8×1.8 mm^2 defined by shadow masks to work as transparent electrodes. The deposition rate plays an important role for Au. Slow deposition introduces isolated Au islands and reduces the conductivity of Au film significantly, thus deteriorates the device performance. A rate higher than 1Å/s is preferred in our case.

4.3.2 Results

Figure 4.6 shows SEM images of the bio-cellulose structures before and after ZnO QD deposition. We can see that the QDs formed a smooth and continuous layer embedded in the cellulose structure. A visual optical transparency comparison between reed membranes and tracing papers before and after ZnO deposition is presented in Figure 4.7a and Figure 4.7b. The reed membrane is more transparent, with $\sim$85% visible light transmission, than the tracing paper ($\sim$65%), as shown clearly in Figure 4.7a. But what's surprising is that it becomes even more transparent visually after the embedment of ZnO QDs, as more details of the background image are preserved. This can be possibly attributed to the waveguiding effect of ZnO. ZnO has a slightly larger refractive index (n$\sim$2) compared to the cellulose (n$\sim$1.47), and thus scattering is possibly reduced in pores and more light is transmitted through channels formed by ZnO QDs. A similar effect is also observed in the tracing paper, but not as significant as in the reed membrane, due to the thicker and denser structure. To confirm the above observation and better understand how ZnO influences the amount of light transmitting through the substrates, especially at the UV range, we measured the light transmittance (T) before and after ZnO embedment and show the corresponding transmittance ratio (T_{after}/T_{before}) versus illumination wavelength in Figure 4.7c for both the reed membrane and the tracing paper. Note that Figure 4.7c is generated from UV-vis transmission data, which may not directly reflect the actual transmittance due to the large optical haze of the material, but it well-reflects the phenomena we observe. We clearly saw enhanced transmission of light at visible range. At UV range the transmittance is significantly reduced for both materials after ZnO QDs are embedded due to the absorption of ZnO QDs, which contributes to UV photodetection.

Photoluminescence(PL) measurements are done on a Horiba FL3-21tau Fluorescence Spectrophotometer. The samples are excited under a wavelength of 365nm, which is the center wave-

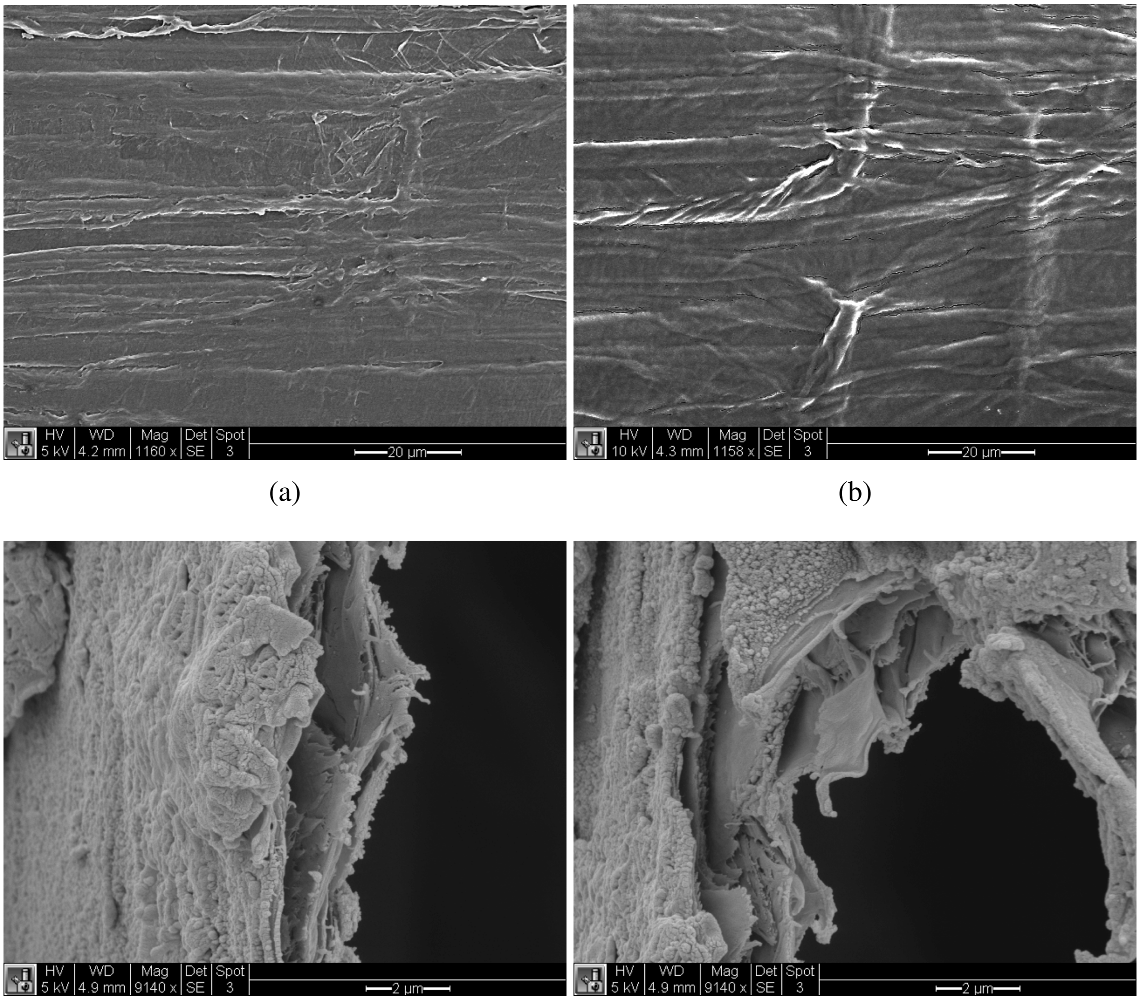

(a) (b)

(c) (d)

Figure 4.6: SEM images of the bio-cellulose structure (a) before, and (b) after ZnO QD deposition; (c) and (d) Cross-sectional views of how ZnO QDs wrap around the cellulose structure.

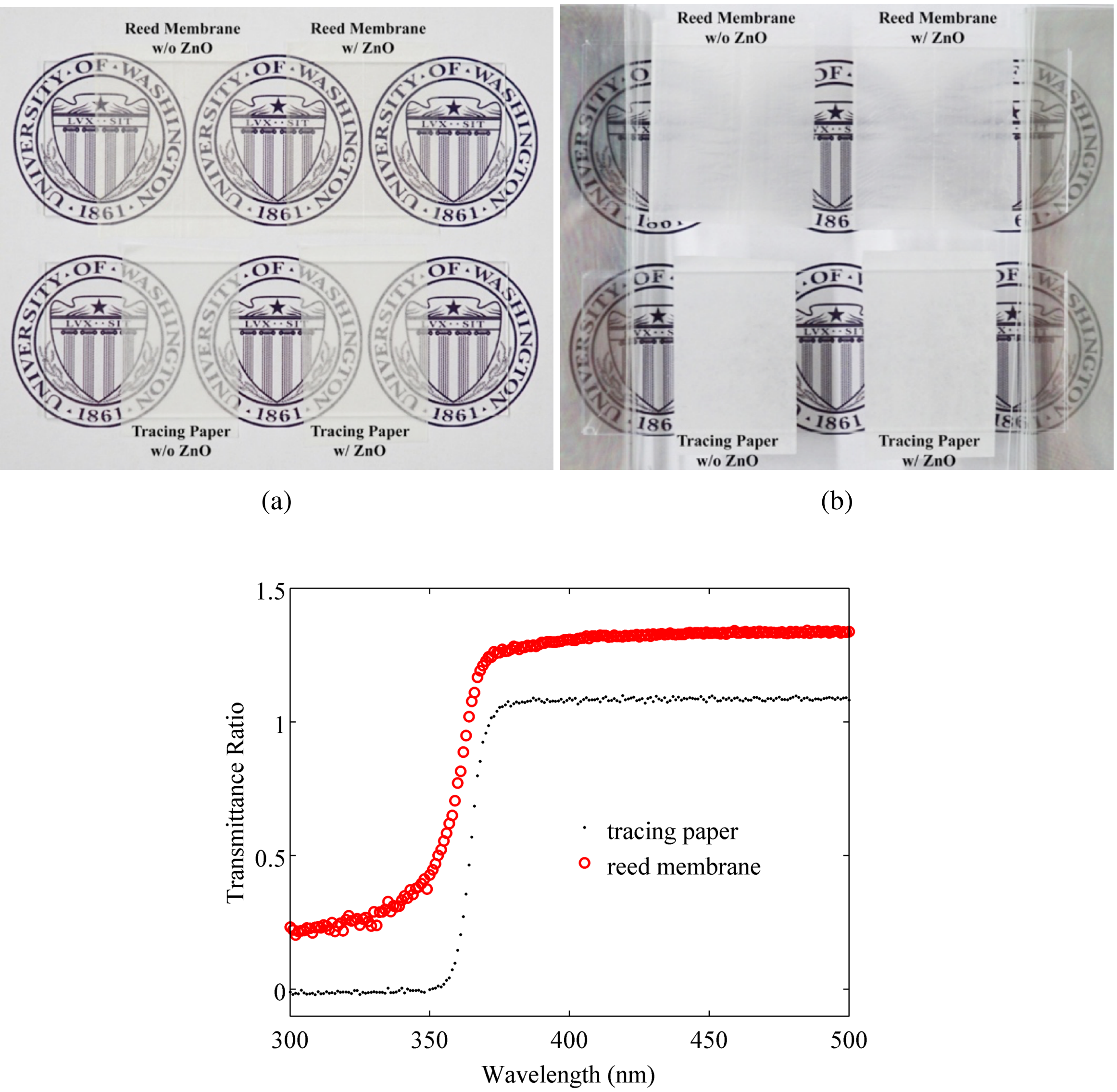

(a)

(b)

(c)

Figure 4.7: (a) and (b) Visual optical transparency comparison between reed membranes and tracing papers, before and after ZnO QD deposition. A glass slide is placed on top of the materials for fixation purpose. The materials are placed a) close to, and b) away from the background image. (c) The optical transmission comparison between the two cellulose materials over UV-visible range. The data shows the ratio of transmittance after ZnO QD deposition to that before the deposition. The transmittance is enhanced in visible wavelengths by the ZnO QDs, but reduced at UV wavelengths due to ZnO absorption as expected.

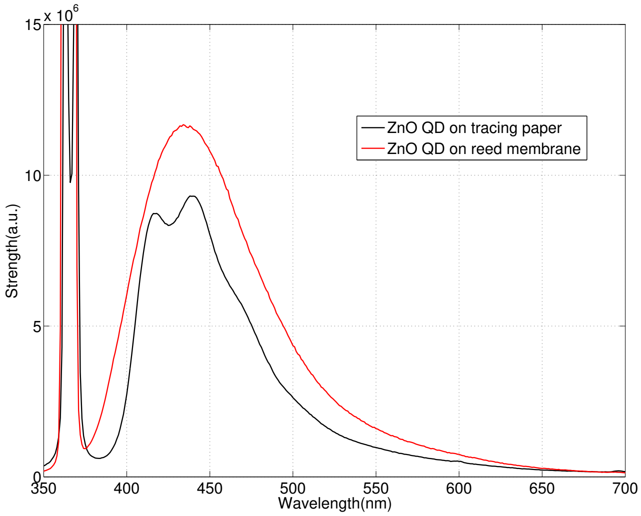

Figure 4.8: Photoluminescence results of ZnO quantum dots embedded in tracing paper and reed membrane. The materials are excited at a wavelength of 365nm, which is a wavelength for common dark lamp light sources.

length for a lot of common UV light sources used in the lab. The photoluminescence spectrum for ZnO QDs embedded in reed membrane and tracing paper is shown in Figure 4.8. While similar response curve shape on both samples are observed, the ZnO QD-tracing paper system turns out to have narrower PL and with a dimple at the peak. These could be due to more scattering and absorption on the material system. It can also concluded that the reed membrane preserved more PL properties of ZnO QD and is more suitable for optoelectronic use than tracing paper based system.

4.3.3 Facile Vertical Structure Performance Test

To check the photoresponsivity of the ZnO-cellulose composite structure before electrodes deposition, I have used a facile sandwich structure with ITO slides and Al foil (Figure 4.9a). ITO has similar work function as gold and thus this structure can operate as a Schottky junction device. The IV responses are shown in Figure 4.9b. A clear Schottky diode response is observed. However, No current is detected at zero bias, and the response doesn't follow perfect exponential curve at higher biases, it might be due to the imperfect contact between the layers.

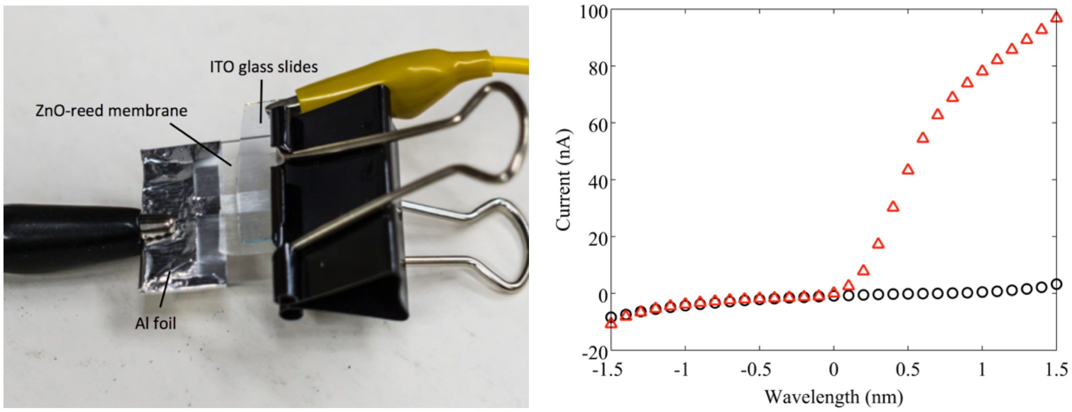

(a) (b)

Figure 4.9: (a) A photo of the ITO/ZnO-cellulose/Al foil sandwich structure for material testing; (b) IV photoresponse results of such a structure.

4.4 Measurement Results and Discussion

4.4.1 I-V Responses

Au thin films of 25 nm thickness with a square pattern size of 1.8×1.8 mm^2 defined by a shadow mask are thermally evaporated onto the ZnO-embedded reed membrane. At such a thickness, the gold layer appears to be of transparent dark green (Figure 4.1a) instead of opaque gold. An Al film of 150 nm is also thermally evaporated on the other side of the reed membrane to serve as the back common contact pad. The current-voltage response of the device is measured under different intensities at 365 nm UV light illumination and the results are shown in Figure 4.10. The I-V curves show Schottky junction behavior. The dependence of the current I on the applied bias V can be expressed by [66]

$$I = I_s[\exp{(qV/\eta kT)} - 1], \tag{4.1}$$

where I_s is the reverse-bias saturation current, q is the net charge of an electron (1.6×10^{-19} C), k is the Boltzmann constant (1.38×10^{-23} m^2 kg s^{-2} K^{-1}), η is the ideality factor of the device, and T is the absolute temperature, which is room temperature (300K) for the experiments. Through

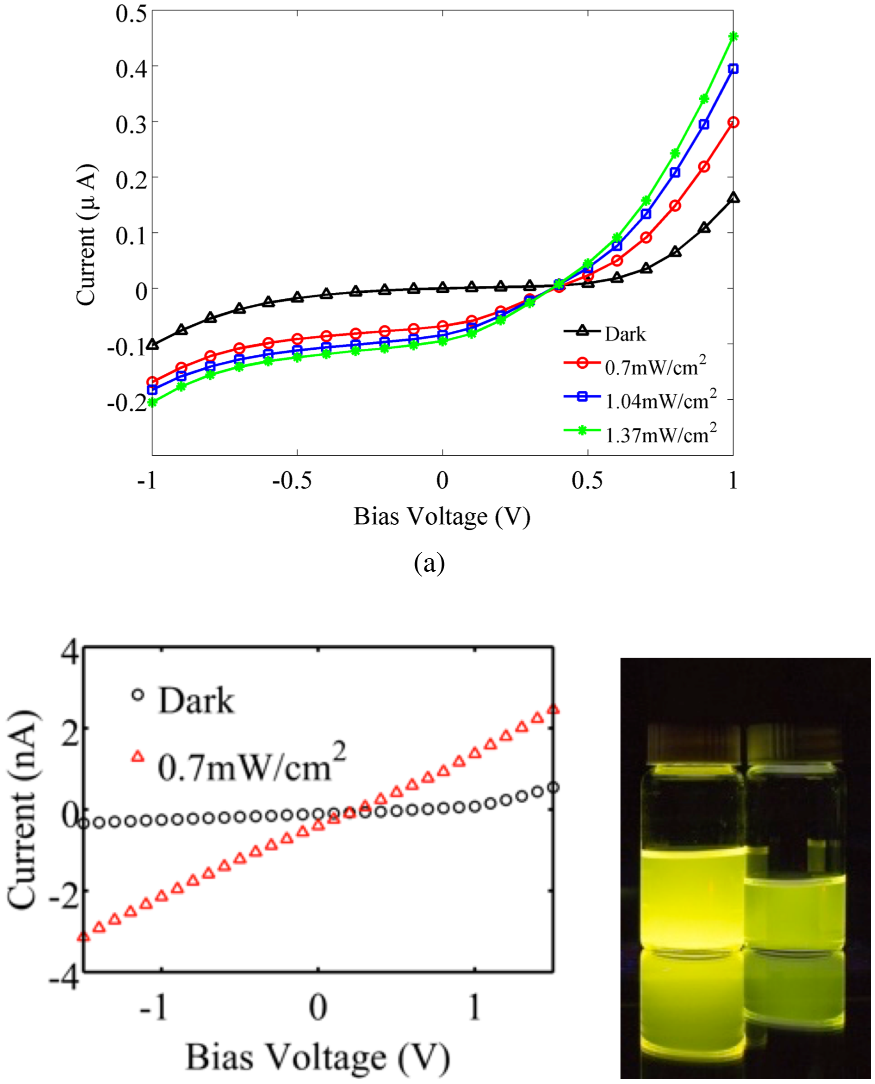

(a)

(b)

(c)

Figure 4.10: (a)Current-voltage characteristics of the UV flexible photodetector on reed membrane under 365 nm light illumination at different intensities; (b) The performance from a similar device fabricated on the tracing paper; (c) The fluorescence from two bottles of ZnO QDs under 365 nm light excitation.

curve-fitting the dark response, we obtained a saturation current of 1.29×10^{-9} A and an ideality factor η of 7.95. While the ideality factor of an ideal Schottky diode ranges from 1 to 2 depending on whether the diffusion current or the recombination current is dominant, our particularly large ideality factor indicates that more mechanisms influence the performance of the device. It is known that crystal defect states and metal-semiconductor interface contamination will lead to large η [67]. ZnO in QD forms are typically prone to having many surface states[72] which greatly influence the optoelectronic properties of the material due to the large surface-to-volume ratio of nano-sized particles. The greenish yellow fluorescence of ZnO QDs under 365nm UV excitation (Figure 4.10c) indicates there are deep level defects in the material. Such large η has also been found from other works in the literature [68, 69] that utilize QDs or other nanostructures, even on rigid substrates. The saturation current can be written as

$$I_s = A_{eff} A^* T^2 \exp\left(-q\psi_B/kT\right), \tag{4.2}$$

where is the Richardson constant (32 A cm^{-2} K^{-2} for ZnO), is the effective device area for illumination, ψ_B is the Schottky barrier height, which is fitted to be 0.83 eV for our device. While it's commonly known that larger n corresponds to lower barrier height due to charge accumulation in the defect states [67], the noticeably large barrier height of our device may be due to the cellulose's insulating nature, which hampers the transportation of the electrons.

Figure 4.10a shows that photovoltaic responses of the device are observed under UV illumination, with an open-circuit voltage of $\sim$0.4V, where all the curves intercept. For energy-saving purpose, it's preferable to operate the device under zero bias. The photoresponsivities of the device under light intensities of 0.7mW/cm^2, 1.04 mW/cm^2 and 1.37 mW/cm^2 at zero bias are 3.7 mA/W, 3 mA/W and 2.5 mA/W, which corresponds to EQEs of 1.08%, 0.87% and 0.75%, respectively at 365 nm wavelength. The slightly decreasing performance at higher intensities is due to the device saturation under more intense light illumination. The I-V curves of a device fabricated on a tracing paper using the same method measured under 365nm UV illumination of 0.7 mW/cm^2 intensity is also shown in the Figure 4.10b for comparison. Despite better conductance of the gold film, it appears to have much lower photoresponsivity performance with more photoconductor-like char-

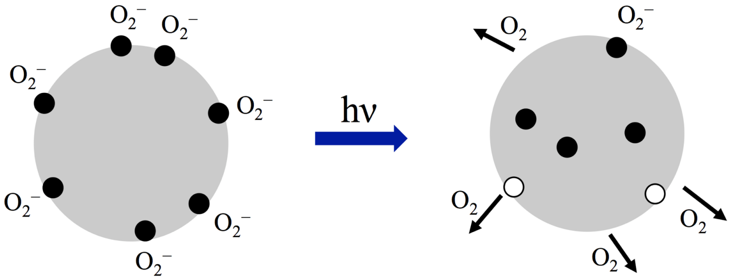

Figure 4.11: Oxygen (a) adsorption and (b) desorption processes upon UV illumination on the surface of ZnO quantum dot. Black dots are electrons and white dots are holes.

acteristics. Because of the dense cellulose structure in the tracing paper, the concentration of ZnO QD is much lower than that in the reed membrane, which hinders the overall performance of ZnO films.

4.4.2 Response Speed

Another important factor that limits the usage of current flexible ZnO UV detectors is the response speed. Most of these devices are made of photoconductive structure, which are typically of low speed due to slow carrier recombination. In addition, the oxygen molecule adsorption and desorption processes [17, 70, 71] in ZnO materials, especially for QDs, further reduces the response speed. In dark, oxygen molecules are adsorbed by ZnO QD and combined with free electrons on the surface [$O_2(g) + e^- \rightarrow O_2^-(ad)$] (Figure 4.11a). When free electron-hole pairs are generated upon UV light illumination in ZnO QD photoconductors, holes are trapped by the oxygen surface states [$O_2^-(ad) + h^+ \rightarrow O_2(g)$] (Figure 4.11b) and leave free electrons circulating the circuit before re-adsorbed by the oxygen molecules or recombine with holes. Due to the involvement of oxygen molecule in the process, it takes longer time to reach equilibrium and thus slows down the response speed. However, in Schottky junctions charge carriers are quickly extracted by the build-in potential in the narrow depletion region upon excitation at zero bias. Hence Schottky junction devices in general have much faster response speed, as demonstrated by our device (Figure 4.12). Sub-second response times are observed for both rise and fall curves. Though the oxygen adsorption

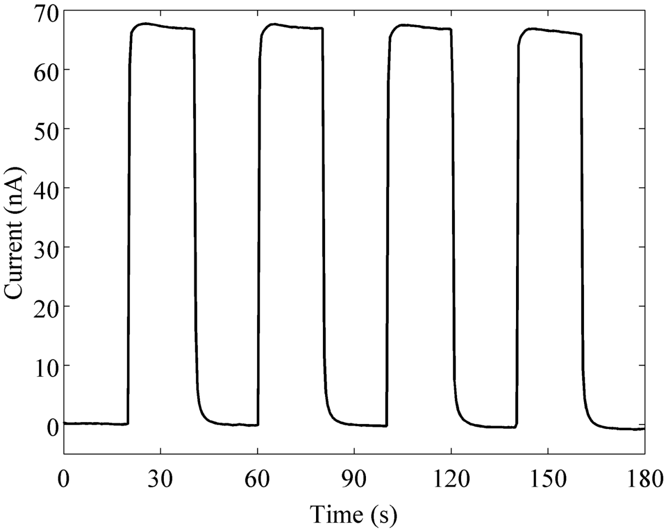

Figure 4.12: Time-response of the ZnO quantum dot UV detector on cellulose structure.

and desorption processes also play a role in Schottky devices by influencing the barrier height of the junction, their impact on the response time is not as significant as that in a photoconductor. But we do see a slower decay rate than the rise rate, which may be due to these processes.

4.4.3 External Quantum Efficiency Measurement

The monochromatic light is obtained from the the setup shown in Figure 4.13. A monochromator is used to select a single wavelength of light out of the broad bandwidth white light from the tungsten light source. Since the UV light is just a very small portion from the tungsten light source(Figure 4.14), we need to focus the light into a small spot to achieve maximum light utilization. The light then go through a collimating lens pair and focusing lens pair to converge the light to the sample.

The spectral-wise EQE measurement result of the cellulose device is shown in Figure 4.15a. The device performance peaks at $\sim$350 nm with EQEs over 3%, which corresponds to photoresponsivities of >8.5 mA/W. The photoresponse cuts off gradually at $\sim$375 nm, which corresponds well with the bandgap of bulk ZnO. However, the absorption curve of ZnO QDs in solution form (Figure 4.15b, black curve) shows a sharp cut off at $\sim$360 nm and flatter UV absorption, which

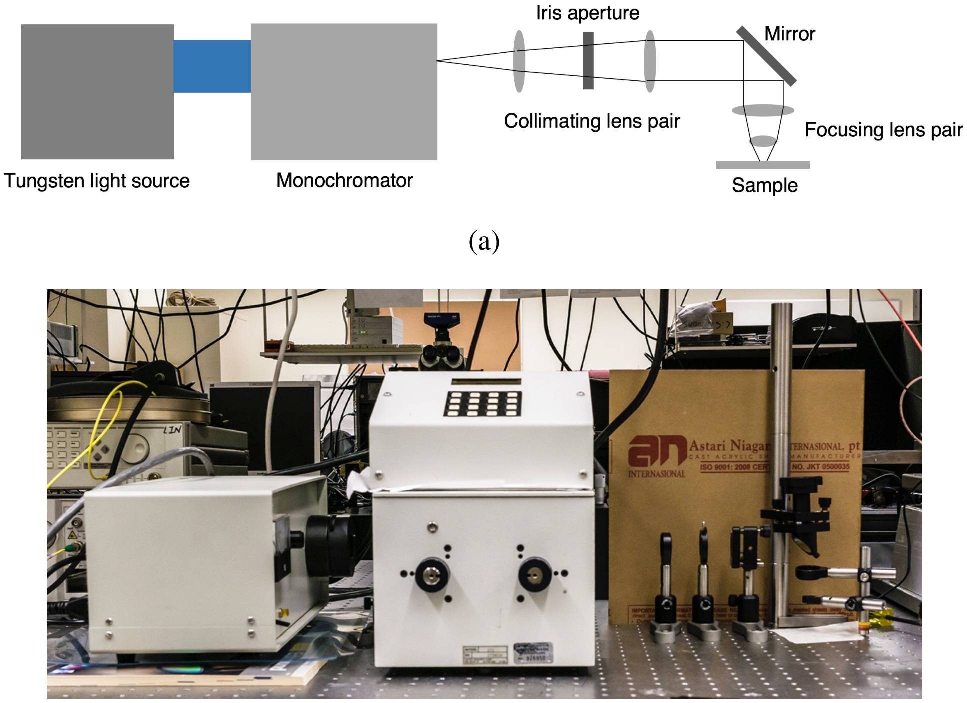

(a)

(b)

Figure 4.13: (a)A schematic of the external quantum efficiency measurement setup and (b)A photo of the real setup.

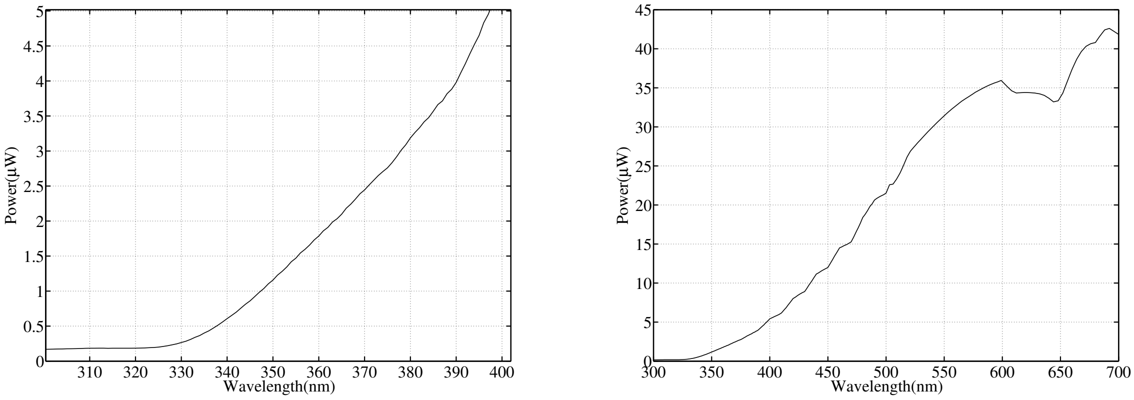

(a)

(b)

Figure 4.14: Light power illuminating on the photodetector: (a) A close look at the wavelength range from 300nm to 400nm; (b) From 300nm to 700nm.

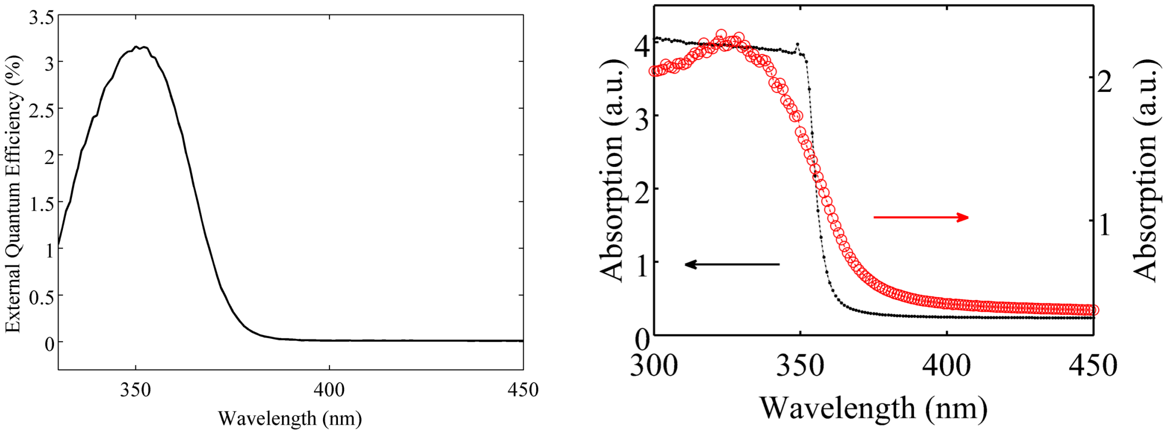

(a) (b)

Figure 4.15: (a)EQE curve of the device; (b)ZnO QD absorption spectra; the black and red curves correspond to ZnO QD in solution and on reed membrane, respectively.

is understandably due to quantum size confinement. The discrepancy may be due to the agglomeration of the ZnO QDs when deposited on the reed membrane, which results in a more bulk-like energy bandgap structure. To verify this, we performed absorption measurement of ZnO QDs on reed membrane, and the result is shown as the red curve in the Figure 4.15b, which exhibits a trend similar to the EQE curve. The blue shift of the peak is due to the absorption of the reed membrane, which accounts for the decreasing performance of the photodetector at deeper UV range. No response is observed at visible range, which indicates that this device functions as a naturally visible-blind UV detector.

Table 4.1: Comparison between UV detectors in the literature

Material[1]	Structure (PC/PD)[5]	Flexible (Y/N) [s]	Rise/fall time[2] [mA/W]	Photoresponsivity[3] [V]	Bias voltage [nm]	Wavelength[4]	Ref
ZnS-ZnO	PC	Y	0.77/0.73	<1	10	320	[72]
ZnO NW	PC	Y	>400	>1A/W	3	-	[73]
ZnO-rGO	PC	Y	6/3.5	<<1	10	365	[74]
TiO_2	PC	Y	1.4/6.1	16	1	345	[75]
SnO_2	PC	Y	>20/>50	230	5	320	[76]
ZnO NW	PC	Y	19.6/2.5	8.3	0.5	365	[77]
ZnO-Au NP	PC	Y	∼40/>56	1.51×10^5	50	350	[78]
TiO_2	PD	N	0.15/0.05	25	0	350	[79]
ZnO/p-Si	PD	N	<0.3	408	0	355	[80]
ZnO-organic	PD	N	0.2ms/0.95ms	0.017	0	390	[81]
ZnO NW	PD	N	81ms	1.82	0	365	[82]
ZnO NR-CuSCN	PD	N	0.5μs/6.7μs	7.5	0	355	[83]
Organic	PD	N	20ns/888ns	22.5	0	350	[84]
ZnO NC	PD	Y	∼0.5/∼1	>8.5	0	350	This work

4.4.4 Comparison with Other Devices in the Literature

Table 4.1 shows the device performance comparison among various UV photodetectors reported in literature and this work. Both flexible devices and rigid devices with photodiode structures are included. Our device shows faster time response than most of these flexible devices with photoconductor structures and at the same time offering comparable performance in photoresponsivity under zero bias. Compared to rigid p-n or Schottky junction-based devices, the photoresponsivity is comparable while the response speed is understandably slower due to the structure and thickness of the cellulose material. Overall, our device balances the response speed with photoresponsivity, while at the same time offers flexibility with a simple fabrication process.

---

[1] NW stands for nanowire, NR for nanorod and rGO for reduced graphene oxide;

[2] Different work might use different models for response time calculation based on experimental data;

[3] Some of the results are calculated based on the given information from the reference;

[4] It's the wavelength resulting in the maximum photoresponsivity.

[5] PC stands for photoconductor, and PD stands for photodiode;

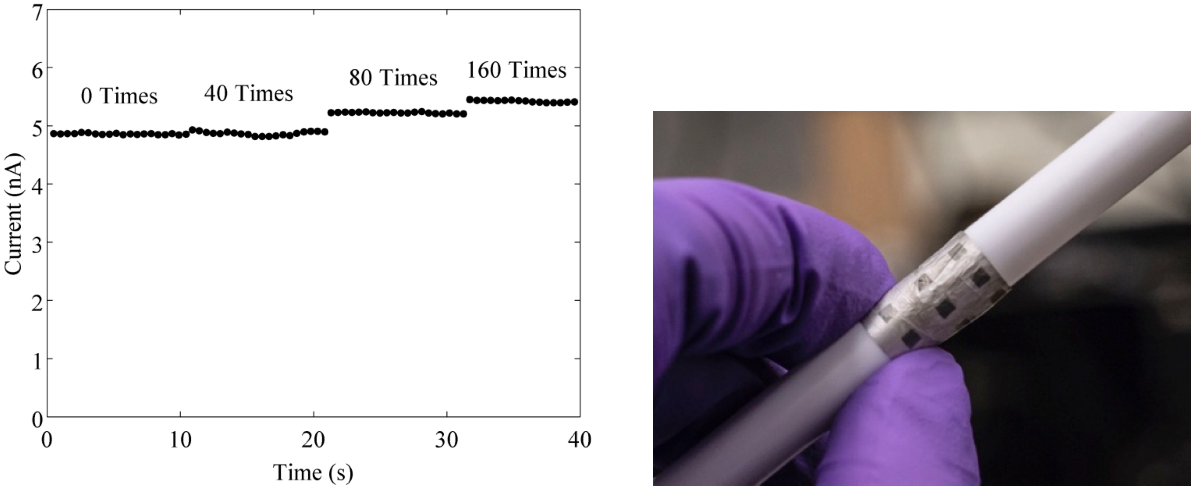

(a)

(b)

Figure 4.16: (a)Bending test results of the device; (b) photograph of the device bending around a pen. The devices are under 365 nm light illumination with intensity of 65 μW/cm^2.

4.4.5 *Bending Test*

Being a flexible device, the UV detector performance should not degrade due to bending. The device performance under different numbers of bending cycles is measured and the results are shown in Figure 4.16a. Measurements are taken after 0, 40, 80 and 160 bends around a pen with a radius of 4 mm (Figure 4.16b) under an illumination intensity of 65 μW/cm^2 at 365 nm wavelength. The photocurrent over 10 second time period after each bending is plot in the figure. A slight performance increase is observed after each bending. Since the device was tested without rest after bending, it's possible that the cellulose structure was under compression, which squeezed the NCs and facilitates the carriers to tunnel through nearby NCs, and thus improved the overall conductivity of the ZnO NC film. To further understand the the effect of bending on the device performance, we tested a device under different bending radii, and the results are shown in Figure 4.17a. The photocurrents over 80 second time period at bending radii of infinity (flat condition), 10mm, 9mm, 7mm and 6mm (over a stainless steel object (Figure 4.17b)) under an illumination

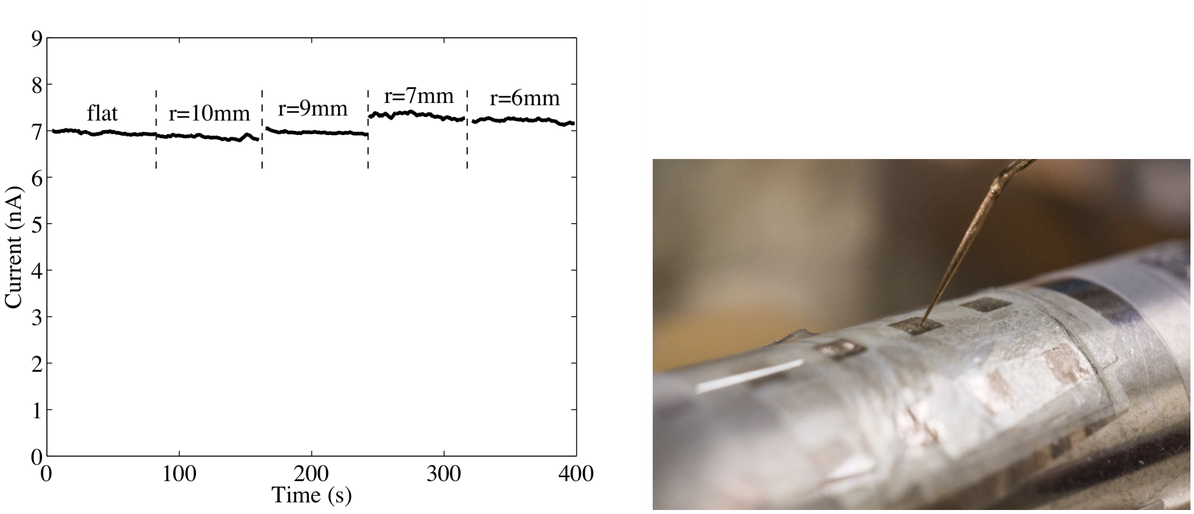

(a)

(b)

Figure 4.17: (a)Device performance at different bending radii; (b)A photo of the device under test on a cylindrical stainless steel object.

intensity of 76 μW/cm^2 at 365 nm wavelength are plot in the figure. Overall, slight photocurrent increase was observed at smaller bending radii, which is in accordance with the previous bending cycle test results.

Chapter 5

FREESTANDING ULTRATHIN ZNO QUANTUM DOT-NANOFIBRILLATED CELLULOSE FILM FOR SUBSTRATE-FREE UV PHOTODETECTORS

While we are able to increase device performance by using reed membrane instead of tracing paper, the membrane is still a limiting factor. The membrane is much thicker than normal active layer thickness, which is of several hundreds of nanometers, and greatly deteriorate the carrier transportation. The irregular hierarchical structure of the membrane and large size microfibril clusters also renders roughness on the membrane surface and increases the absorption by the membrane. These can all be overcome by moving to nanofibrillated cellulose(NFC). As is introduced in Chapter 2, nanopaper has superb mechanical and optical properties that is suitable for optoelectronic applications. However, to achieve high transparency and smoothness, NFCs should be tightly bond to each other and left little room for embedding quantum dots(QDs). This problem can be solved by using NFC as the structuring material to form a freestanding ZnO layer, i.e., making QD-NFC composite fibers and made ultrathin papers out of it. Further literature research reveals previous work on functionalizing nanopapers with other nanomaterials. Eden Morales-Narváez et al. has incorporated metal nanoparticles and used if for sensing [45]; Yuanyuan Li et al. mixed Fe_{34} nanoparticles with NFC and made magnetic papers out of it [47]; Juan Xue et al. created ZnSe-NFC structure for photoluminescence purpose [48]; conductive paper are also made possible by incorporation of silver nanowires [6,42]. However, no ultrathin ($<1\mu$m in thickness) nanopaper is made available so far. Thick paper structure also significantly reduces the transparency of the paper.

In this chapter, I'll talk about the fabrication process we developed to fabricate ultrathin, ultraflexible and transparent ZnO-NFC membrane, as well as the device we made out of these membranes.

5.1 Ultrathin ZnO Quantum Dot-Nanofibrillated Cellulose Membrane

A simple nanopaper making process consists of NFC preparation, filtering and drying. The wood cellulose pulps are disintegrated into NFCs by running through a microfluidizer under high pressure after TEMPO-mediated oxidation. Then the NFC water suspension is filtered in vacuum filtration to form a wet gel "cake". The cake's peeled off from the filter and dried under a drying setup to form a paper. In order to make ultrathin ZnO QD-NFC membrane, all these steps needs to be re-engineered.

5.1.1 ZnO QD-NFC Preparation

Roughly there are two kinds of mixtures for ZnO QD and NFC suspension, one has perfect phase matching for these two materials so they can suspend evenly in solvent, another is to bind these two together to form ZnO QD-NFC composite fibers. However, in view of the filtering process, the former could results in great loss of ZnO QDs. NFCs are fibers with a length from 10s of nanometer to several micrometers that can easily form a cohesive gel cake after filtration, while ZnO QDs are near-perfect inorganic crystals that have a diameter of less than 10nm that could easily be flushed away during filtration. Thus only the latter method should be used and luckily that's also what we have from the original material. Colloidal ZnO QDs synthesized from the wet-chemistry method used in Chapter 4 have hydroxyl groups on the surface, which helps the QDs to suspend in water and also opens up room for functionalization. NFCs obtained by TEMPO-mediated oxidation have carboxyl groups on the surface that also help with the suspension and functionalization [47]. A composite structure can be obtained by interactions between carboxyl groups in NFCs and hydroxyl groups in ZnO QDs.

For device application, we would want the concentration of ZnO QDs to be as high as possible, but it's not as simple as adding a lot of QDs into NFC suspension. Due to the interaction between hydroxyl and carboxyl groups, the QDs and NFCs will form a bigger cluster. And due to

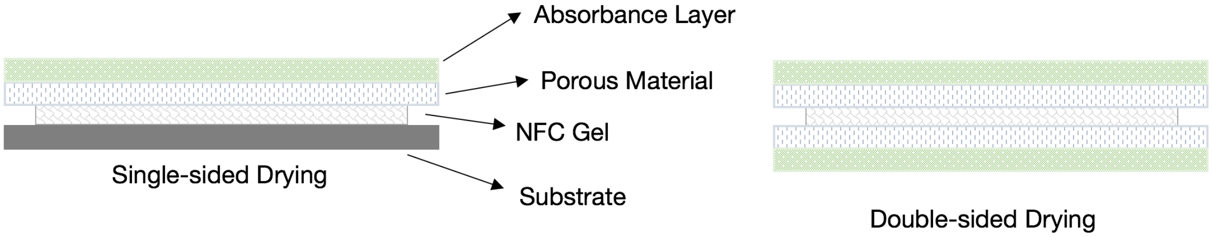

Figure 5.1: Schemetics of single-sided drying method and double-sided drying method.

depletion of these charged groups upon exposure to too many QDs, the clusters will agglomerate to form clouds and precipitate out. Even regional over saturation of QDs during mixing could lead to precipitation. By adding the QD suspensions to NFC suspension dropwisely and stirring the solution rigorously during mixing, we are able to suspend the clusters more evenly. However, it cannot solve all the problems. There are still precipitations formed since stirring cannot break the clouds that are already formed. Thus higher energy methods such as ultrasonication equipments need to be used. Ultrasonication bath can be used to make a mixture of low ZnO to NFC mass ratio (∼0.5:1) and higher ratios can be achieved by using ultrasonication homogenizer.

5.1.2 Drying, and Solvent Exchange

The vacuum filtration technique should be standard due to its relatively simple principle. After forming a wet gel on the filter, it needs to be dried to make a paper. Typically there are two ways to dry a wet cellulose gel, single-sided and double-sided, as shown in Figure 5.1. For single-sided drying, one side of the NFC gel is attached to a flat substrate with another side covered by some porous materials, such as woven mesh cloth, and a solvent absorbance layer. In this way, the water or other solvent can only leave from one side. For double-sided drying, both sides of the gel are covered by the porous material and absorbance layers so that the gel can be dried from both sides. For a thick paper, both methods yield good results. However, for an ultrathin film, things are more complicated.

Water has very strong capillary forces due to hydrogen bonding between molecules on the NFCs that can easily bend the ultrathin gel if there's no support. The bend is almost irreversible because by contacting each other, the gels are inseparable, again due to the water capillary forces. So it's very difficult to freestand the gel in air and we need a supporting layer to flatten it out. So should we use single-sided drying? A quick answer is no and the story doesn't end here. For a large area of gel, it's basically impossible to have the same evaporation rate for all local regions on the surface, which means that there will be uneven distributions of solvents in the gel during the drying process. Tight-binding between nanocellulose due to high surface-volume ratio also renders it hard to evaporate the water. Again the capillary force will also be localized and break the whole gel into pieces. Furthermore, being ultrathin, the binding force or cohesion force between nanocelluloses could be smaller than the Van der Waals forces between the nanocellulose and substrate, and this makes it hard to peel off even after drying. Therefore we need to use double-sided drying method and we need to be able to freestand the gel, which basically means that we have to overcome the capillary force from the water and leaves us with the option to do a solvent exchange with a liquid with much less capillary force, such as isopropanol(IPA).

One might point out that the filter could be used for drying and supporting the gel. While both of these functions could be achieved, it's not as simple as drying it immediately after filtering on the same filter. Because the NFCs could enter the pores in the filter and form roots, which prevent ultrathin papers to be separated from the filter. Thus we need to transfer the gel to another substrate first and then freestand it with IPA. We then need to choose the substrate. After testing a bunch of substrates such as glass, stainless steel and acrylic, we found acrylic works best. The transfer process could be complicated to describe, so we can start from the solvent-exchange process. Due to the fragileness of the ultrathin gel cake, even with the solvent exchange, it's still very possible that we can break it by suspending it in the air. Thus it would be better to have all the processes done in solvent, which is IPA in this case. So basically what we do is to soak the gel with the substrate in IPA. In order to separate the gel from the substrate, we would want a complete solvent exchange with IPA accessing the gel at all the directions. One way to do this is through using porous substrate, but it could lead to uneven film morphology during the transfer process. Another

(a) (b)

Figure 5.2: (a)IPA droplet wets completely on an acrylic plastic surface; (b)IPA droplet wets incompletely on a stainless steel plate and forms a finite contact angle with the surface.

way is to find a substrate surface that has perfect wettability of IPA. From very simple solvent droplet test, we figured that IPA can spread out on acrylic without any effort. Figure 5.2 shows how IPA droplet wets on stainless steel and acrylic plastic surfaces. IPA's able to wet completely on an acrylic plastic but only covers a small area on stainless steel. Wetting of a surface could be a very complicated process that may relates to many kinds of forces such as Van der Waals, static electric, chemical bonding forces [85]. For simplicity, if we just look into Van der Waals force, this could relates to the surface energy and polarity of the surface and liquid. Materials like metals and glass are of hard solid, which are made of ionic, metallic or covalent bonds, and the wettability of such surface is determined by the polarizabilities of the surface and liquid. A higher polarization surface could wet the liquid better. However, for something like water, which is a solvent that has high polarity, it cannot wet a lot of untreated hard solid surfaces. Glass is an exception cause it has hydroxyl groups on the surface due to oxide nature and can form hydrogen bonds with water. For IPA, even though it has lower polarity than water, it's still higher than stainless steel and still form a finite contact angle on the surface, though smaller than water. For soft solid, which are formed by Van der Waals force or hydrogen bonding, such as acrylic plastic, we can look into the critical surface energy. IPA has a surface energy (∼23mN/m at 20°C) well below the critical surface energy of acrylic(∼37.5mN/m), this gives it perfect wettability on acrylic.

With the substrate decided, we can look into the transfer process. We can compare between the parameters $G_{filter/gel}/G_{gel/acrylic}$, which is a measure of the interfacial adhesive strength between filter and gel cake/gel and acrylic, respectively. Ideally, we would want $G_{filter/gel} < G_{gel/acrylic}$. Intuitively we would look into static cases that the filter peeling off process is done slowly and carefully. Under such case, we only need to consider the work of adhesion W_{sl}, as the work must be done to separate two adjacent phases s(olid) and l(iquid), which is given by the Young-Dupre equation [86]

$$W_{sl} = \gamma_l(1 + \cos\theta), \tag{5.1}$$

where γ_l is the surface energy of liquid and θ is the contact angle. The contact angle is related to the wetting properties of the substrate surface given a liquid. Water has very high surface energy and results in terrible wettability on a lot of surfaces. We found water has big contact angle on acrylic and $W_{gel/acrylic}$ could be small. However, we use hydrophilic filters to do the filtration, which has very good adhesion to water. Thus to improve adhesion, we need to dry the water a bit to reduce the capillary force between the filter and the gel. But it doesn't solve all the problem. It could still be hard to peel off the filter since $W_{gel/acrylic}$ doesn't dominate. What we found in the experiment is that the faster the peel, the better the quality of the gel film. However, we found the transfer printing energy release theory [87] is contradictory to our finding, under which the adhesion is positively depending on the peeling velocity. Nevertheless, it turns out that the capillary force is also dependent on the velocity of how surface moves [88, 89]. If we take the porous feature of the filter into consideration, it's possible that during the peeling off process, there's abrupt change in the contact between water and the filter at the cracking tips. So that there's rebuilding or redistribution of the capillary force at that area, which is then similar to the cases in Reference [88, 89].

After figuring out how to freestand the gel, we still need to find a way to dry it. Porous materials need to be placed on both sides of the gel in order to leave channels for evaporation of solvents. Since we are focusing on making membranes with thickness less than 1 μm, the surface needs to be very smooth and the pores need to be very small (likely <1 μm). That left us with options of filters. PVDF filter with a pore size of 0.1 μm turns out working pretty well with both the smoothness and pore size meeting the requirement. It also stays well in IPA. Cellulose acetate filter was also a candidate, but it turned out that NFC has strong cohesion force with this material due to similar chemical composition and results in inseparable films.

5.1.3 Summary on Paper Making Processes

The whole paper making process is summarized and shown below.

NFC making: 78mg TEMPO is dissolved in 100ml DI-water and mixed with 514mg NaBr after it's been dissolved in 50ml DI-water. The mixture is added to 5g dry bleached softwood pulp with 65ml DI-water. The pulp should be cut or torn into little pieces for better contact with all the chemicals. After all these, add 30ml $\sim$12% NaClO to start the oxidation with strong magnetic stirring. The pH of this reaction is monitored every 15mins and controlled to be $\sim$10.5 with 0.5M NaOH solution. Stop adding NaOH after 2.5 hours but keep stirring the mixture for another 2hrs or simply overnight for more complete oxidation so that no big pieces of pulp could be seen in the mixture. Use B$\ddot{u}$chner filtration to drain all the solutions out of the end product and wash with DI-water multiple times until it's all white. Suspend the product in 500ml DI-water to create 1wt% dispersion of oxidized cellulose. Disintegrate these celluloses into NFCs by going through a microfluidizer(Microfluidics, Inc. M-110P) at 26,000psi. The NFC suspension is stored at 4°C.

ZnO QD-NFC mixing: The ZnO QDs are synthesized through the same wet-chemistry process described in chapter 4, but stored in MeOH under 4°C. The concentration is $\sim$34mg/ml. It's diluted with DI-water to $\sim$1mg/ml before use. NFCs are diluted to 0.1wt% in DI-water and degassed for half an hour before mixing. To make a mass ratio between ZnO and NFC of 1:1, the same amount of ZnO QD and NFC suspensions are mixed in a glass bottle and sonicated for 5mins with a ultrasonic homogenizer(Biologics, Inc., Model 3000) with 30% power, 30% pulse duration and ice cooling on the outside of the bottle. The product then centrifuged under 2000rpm for 10mins to precipitate out the larger clusters. The supernatant is then diluted again to half concentration by adding DI-water and the resulting solution can be readily used for paper making.

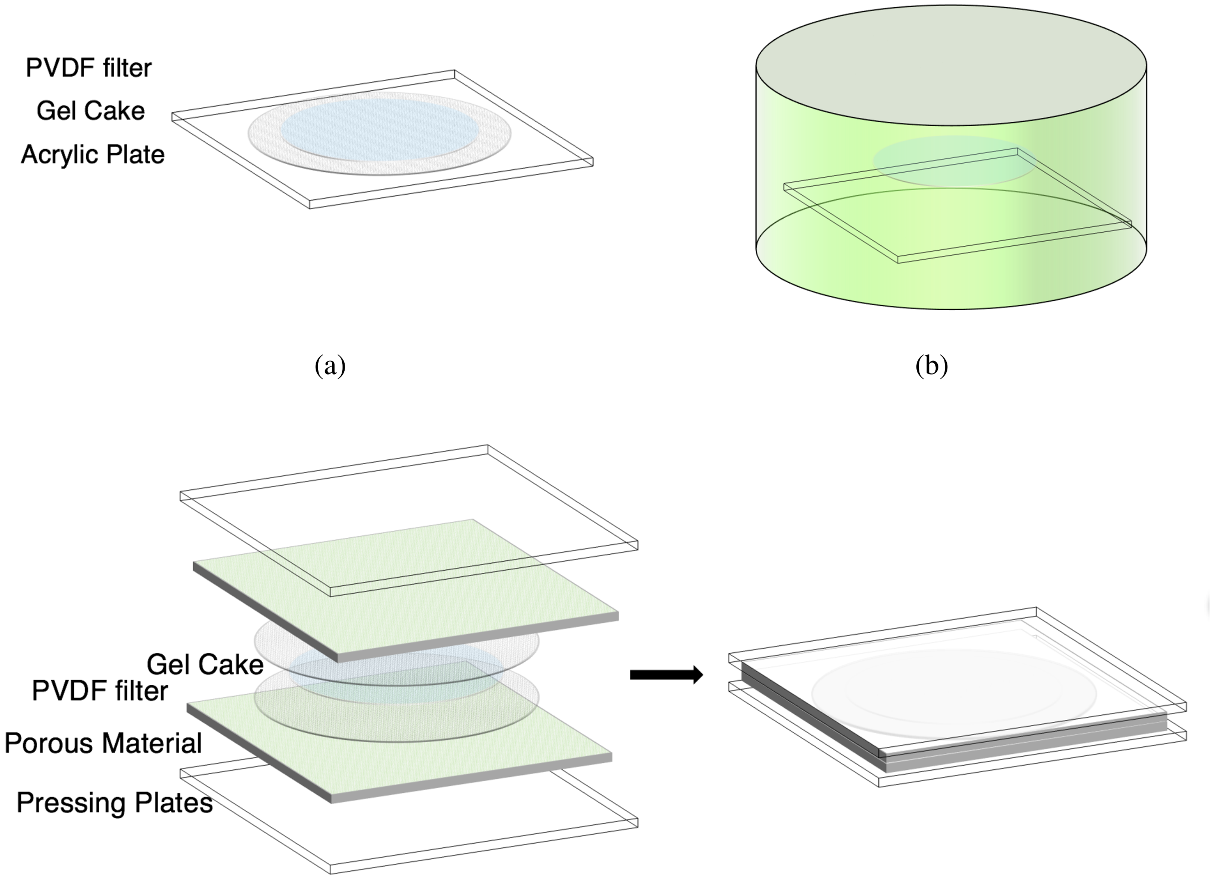

(a) (b)

(c)

Figure 5.3: (a)Peeling off the filter through a transfer printing process to leave the gel cake on an acrylic plastic plate. (b)Solvent exchange and floating of the gel cake by soaking the gel/acrylic structure into the IPA. (c)Drying of the floating gel between two PVDF filter and sandwiched between porous materials and under pressure for smoothing the ultrathin membrane.

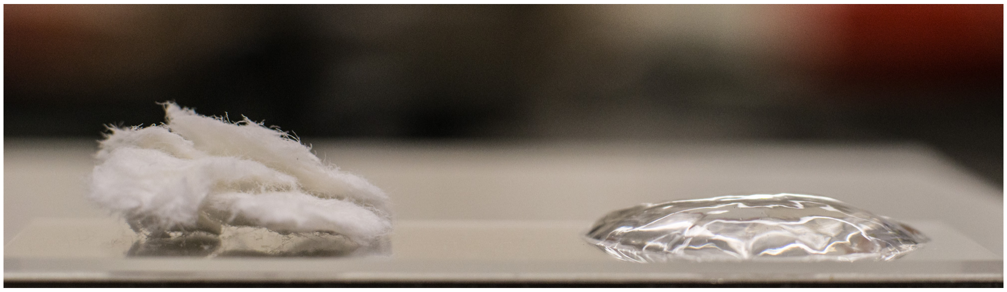

Figure 5.4: From bleached softwood pulp (solid, left) to nanofibrillated cellulose hydrogel (1wt% in DI-water, right)

Paper Making: 3.5ml (could be different depending on the purpose) of above mixture is filtered using a PVDF filter(Millipore, Inc.) with a pore size of 0.1μm. It takes approximately 2mins to do so and an ultrathin wet gel will be formed on the filter. Then the filter's flipped over and the gel's attached to an acrylic plastic plate. After the filter gets a bit drier by using tissue papers to absorb the excess water, lift the filter starting from the edge and peel it off the gel as quick as possible. That will leave the gel cake on the acrylic. Afterwards soak the gel/acrylic structure in IPA and shake a bit to separate the gel from acrylic. After the gel's fully floated in the IPA, spoon it out with a PVDF filter and cover the gel with another. The sandwich structure is then placed between some papers and fixed between two metal plates with pressure. The whole structure is left in a vacuum desiccator overnight for drying. The steps from peeling off of the filter to drying the gel are shown in Figure 5.3.

5.2 Results and Discussion on Material Preparation and Paper Making

5.2.1 Material Preparation

A picture of bleached softwood pulp before any treatment is shown in Figure 5.4 on the left. Microsized fibers can even be seen from the edges. After TEMPO-mediated oxidation and microfluidizing, we obtained the NFC gel as shown in Figure 5.4 on the right. Which is translucent and well-suspended in water. The ZnO QD-NFC composite suspension is shown in Figure 5.5. The solution is pretty translucent under ambient and show yellowish green photoluminescence(PL) under

(a) (b)

Figure 5.5: ZnO QD-NFC suspension under ambient light(a) and UV(b) illumination.

UV illumination. The PL stays for several months which confirms the stability of the suspension. In comparison, ZnO QDs in DI-water lost PL quickly due to agglomeration. Being a structuring material, ideally we would like NFCs to have minimum UV light absorption such that ZnO can have the maximum amount of carriers generated to enhance device performance. We thus looked into the UV-vis absorption properties of the material and the results are shown in Figure 5.6. NFC shows some minor absorption of light at wavelengths shorter than 250nm while ZnO QD-NFC composite shows significant amount of UV absorption. Also by comparing with the ZnO QD absorption spectrum at Figure 4.4, it safe to suggest that a great amount of UV light is absorbed by ZnO QD instead of the NFC. Note that the nonzero absorption for ZnO QD-NFC composite could be from the scattering due to uneven material distribution during sample preparation.

5.2.2 Paper Making

From the material preparation and paper making process described in section 5.1, we are able to make highly transparent ZnO QD-NFC membranes with sub-micrometer thickness. Figure 5.7a shows how transparent is for the paper. We are able to see through the paper very easily without

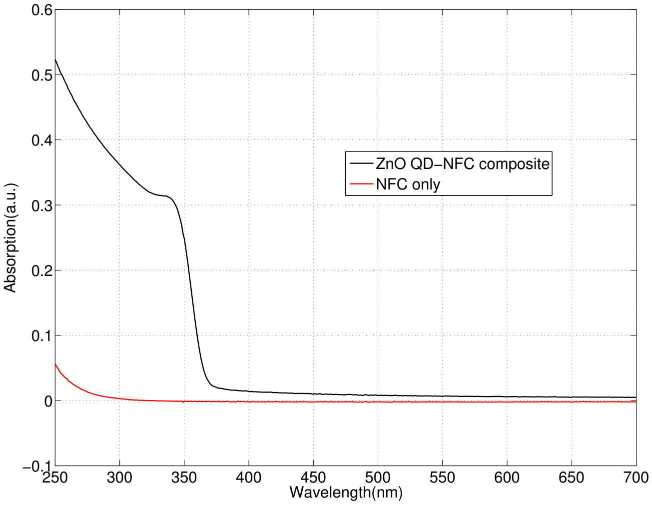

Figure 5.6: UV-vis absorption spectrum comparison between NFCs with and without ZnO QD attachment.

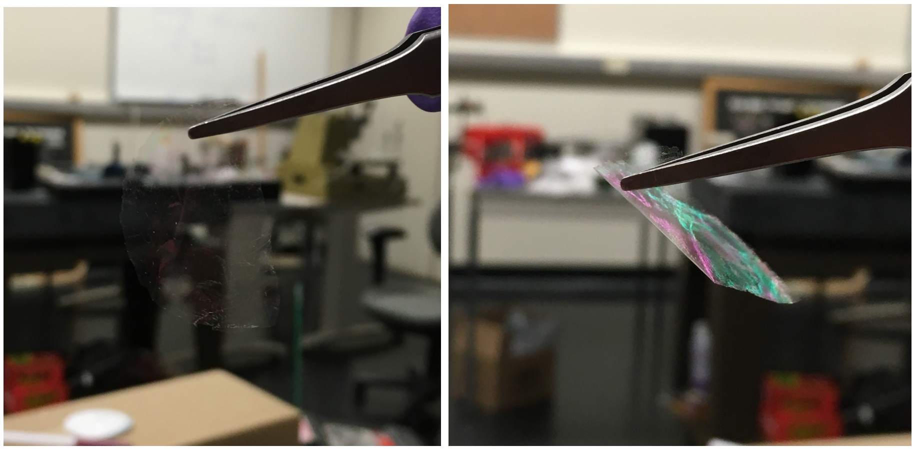

(a)

(b)

Figure 5.7: a) Seeing through an ultrathin membrane; b) Observation of thin film interference at an angle.

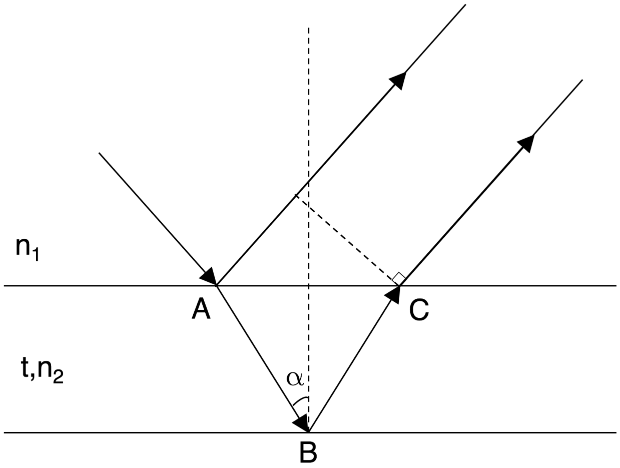

Figure 5.8: A schematic of thin film interference.

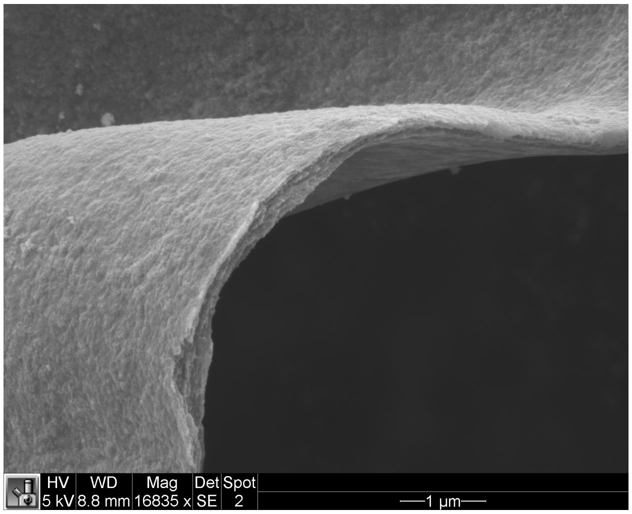

Figure 5.9: An SEM image to show the sub-micrometer ultrathin feature of ZnO QD-NFC membrane.

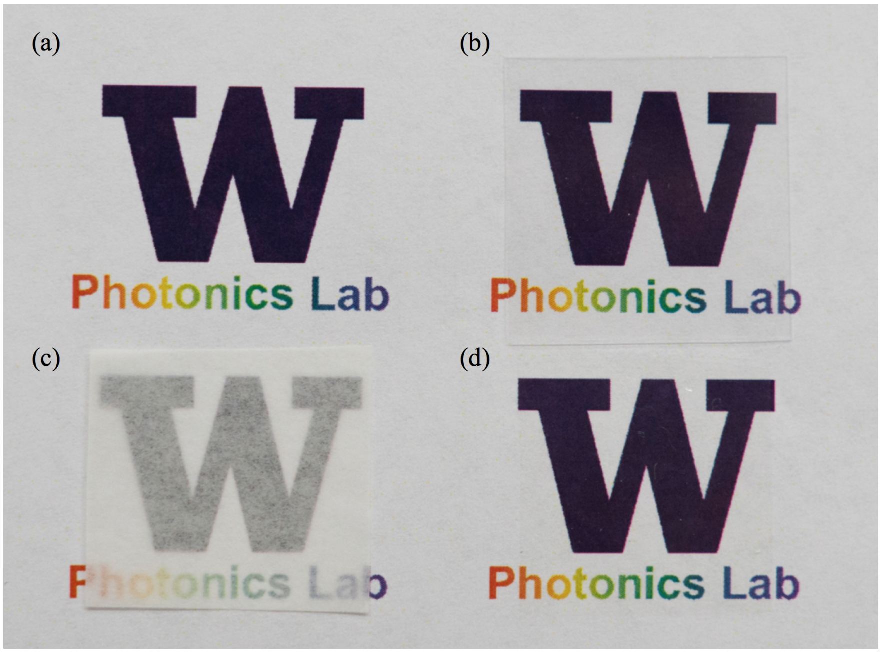

Figure 5.10: Transparency comparison between (a) air, (b) cover slide, (c) tracing paper and (d) Ultrathin ZnO QD-NFC membrane.

any distortion or blurring of the background image, even if it's far away. Figure 5.7 shows the thin film interference when the membrane's viewed at an angle. The principle of thin film interference is shown in Figure 5.8. If the optical distance difference is an integer multiple of the wavelength of light, there will be constructive interference. We can do an easy enough derivation to get the relationship between the constructive wavelengths and the thin film thickness at a certain angle as

$$2n_2 t \cos\alpha = m\lambda (m = 1, 2, 3...). \tag{5.2}$$

m could be larger than 1 if the interferenced light undergo multiple reflections in the film. From the color we observed we can estimate the thickness of the film is at couple of hundred nanometers and it's confirmed in the SEM image shown in Figure 5.9. The membrane is also visually compared with some common transparent or semi-transparent materials in visible light transmittance. From Figure 5.10, we can see that (d), which is our ultrathin membrane, is almost as transparent as the air, and significantly more transparent than the cover slide in (b) and tracing paper in (c). Also due

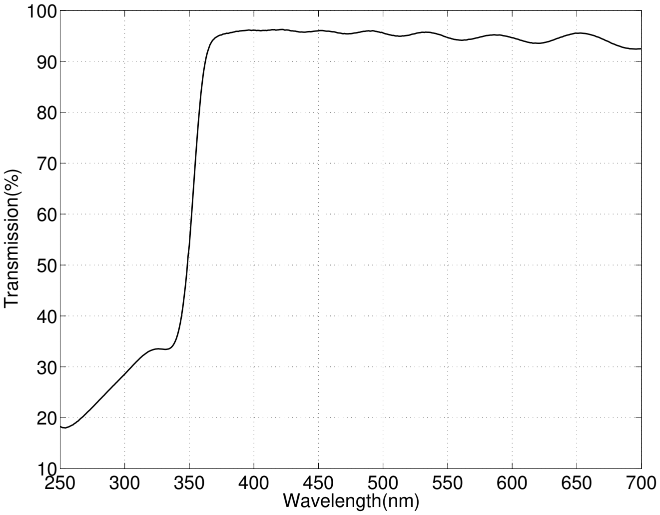

Figure 5.11: UV-vis transmittance of the ultrathin membrane.

to its ultrathin feature, the edge of the membrane can barely be seen. A UV-vis transparency measurement result is shown in Figure 5.11 and we found ∼95% transparency for the whole visible spectrum. For some nanopapers we made, we also see >97% transparency in visible by simply measure it with a calibrated photodetector. By illuminating the membrane with UV light, we can see very bright yellowish green photoluminescence(Figure 5.12) which is exactly the photoluminescence as the composites when in solution form. The PL appears to be pretty uniform throughout the film. The isolated particle-like yellow and blue dots are small paper pieces and dusts, which are attracted to the membrane due to electrostatic charges on the surface.

From the SEM pictures shown in Figure 5.13, we are not able to observe fiberous or porous structures even under a magnification of ∼30000x. This shows that the nanocellulose elements is very small and is close to cellulose nanocrystals. Fairly smooth surfaces can also be observed from the image, also from Figure 5.9. This can potentially lead to good optoelectronic device applications.

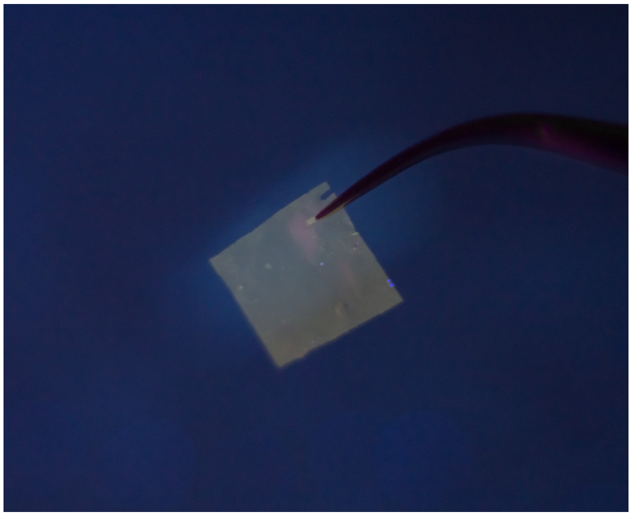

Figure 5.12: Photoluminescence from a small piece of ultrathin ZnO QD-NFC membrane under UV illumination.

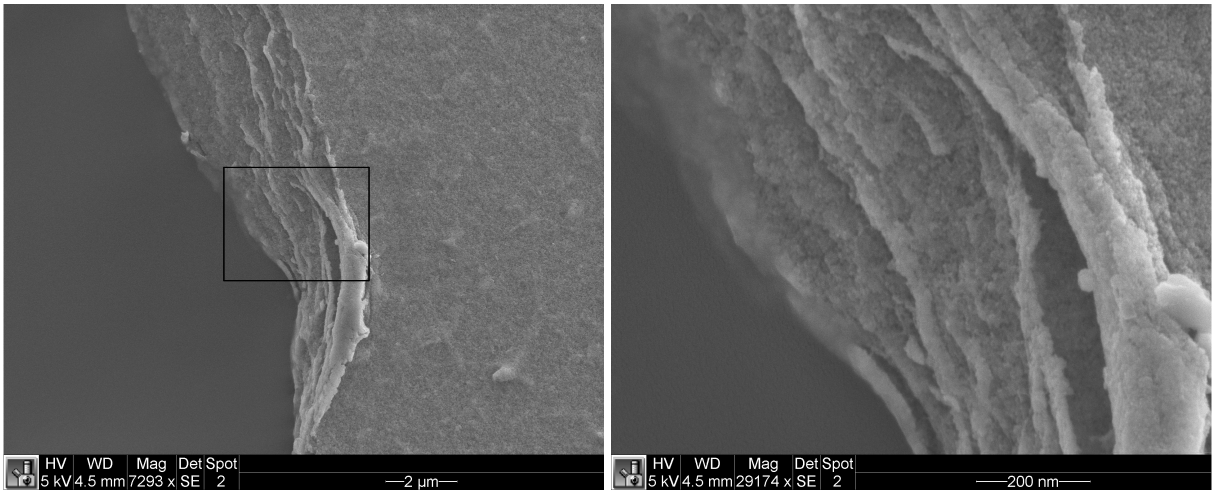

(a) (b)

Figure 5.13: (a)A SEM image showing the smoothness of the ultrathin film; (b)A zoom-in view of the enclosed area in (a) to show the tight structure of the film.

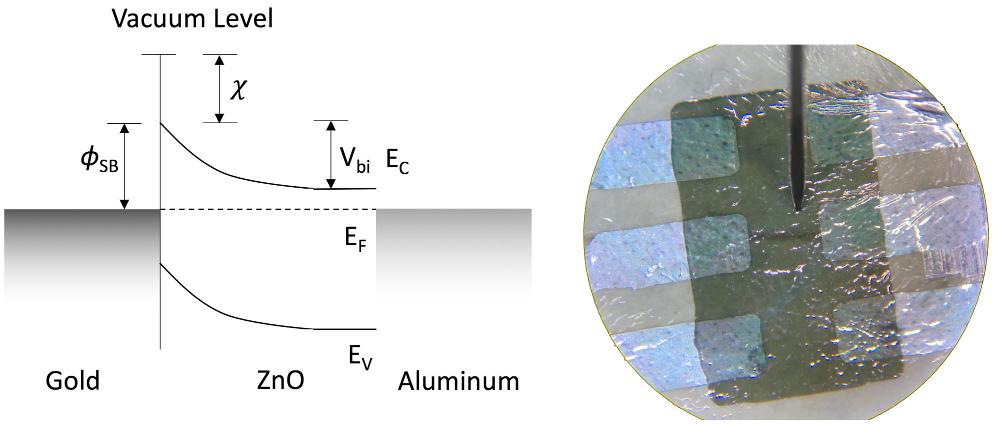

(a) (b)

Figure 5.14: (a)Band diagram of the Schottky photodiode; (b)Schottky photodiodes fabricated on the ultrathin ZnO QD-NFC film under optical microscope. The greenish semi-transparent film is the gold electrode, and the silver pads are aluminum back contact. The overlapping area of the two electrodes are about 2mmx2mm.

5.3 Substrate-free UV Photodetector based on Ultrathin ZnO QD-NFC Film

UV photodetectors are fabricated on the ultrathin ZnO QD-NFC film by depositing other layers and electrodes through evaporation. Two vertical device structures are used and they show distinct behaviors.

5.3.1 Schottky Diode Structure

We fabricated a couple of devices used the same device structure used for the reed membrane device in Chapter 5 (Figure 5.14a). 20nm gold film/100nm aluminum film is deposited through thermal evaporation with shadow mask pattering under high vacuum ($<10^{-6}$ torr) to act as the transparent electrode/back contact, respectively. The gold electrode has a sheet resistance of $<50\Omega/\square$ and is repeatable on different batches of ZnO QD-NFC films, this also confirms the smoothness of the ultrathin film. Being a natively n-type material, a Schottky junction's formed between gold and ZnO. Aluminum has similar workfunction to the Fermi level of ZnO, and the barrier between ZnO

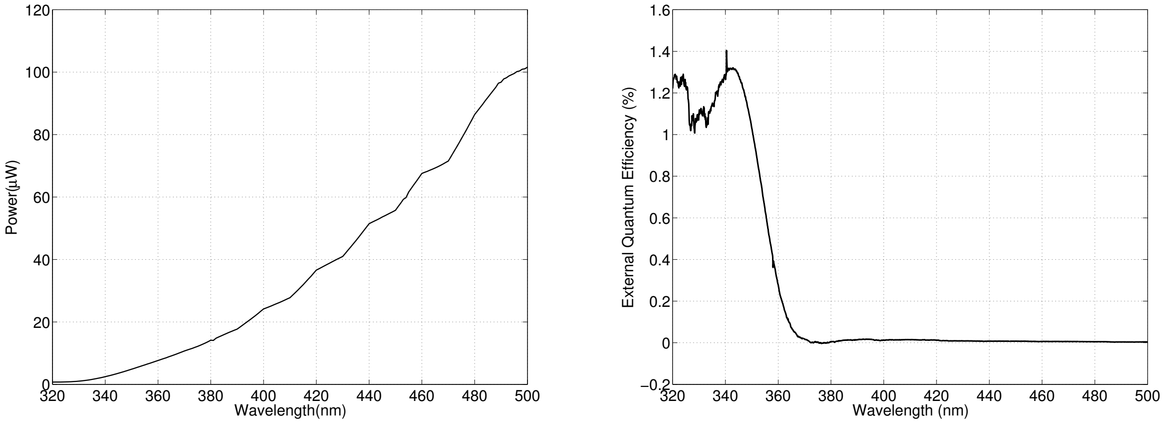

(a)

(b)

Figure 5.15: (a)Monochromatic light power as a function of wavelength used for EQE measurement. (b)The external quantum efficiency of the Schottky diode on an ultrathin ZnO QD-NFC film from 320nm to 500nm at zero bias. A peak is observed at around 343nm, which is close to the bandgap energy of ZnO QD. No response at visible light range is observed. The weak light intensity at shorter wavelengths resulted in noisy response signals.

and Al could be very small and serves more as an Ohmic contact. Thus a Schottky photodiode is fabricated. The actual device is shown in Figure 5.14b. It was viewed under an optical microscope. The greenish pad is the gold semi-transparent electrode and is the illumination side of the device. We can see the aluminum electrodes through the gold electrode and paper.

Just like the Schottky diode on the reed membrane in Chapter 5, this device is also able to operate under zero bias and act as a self-powered UV detector. We tested the external quantum efficiency(EQE) under zero bias and scanned from 320nm to 500nm. The light power in this range is shown in Figure 5.15a. The EQE curve is shown in Fiture 5.15b with a peak response at around 343nm, which is close to the bandgap energy of ZnO QD. The noisy response at shorter wavelengths is most likely due to the small optical power at these wavelengths, which enhances the influence of the electrical noises in the device. Little to no responses are observed at wavelengths longer than 370nm, which is the absorption cut off for ZnO material. Though typically there's still response even when the energy of the photons goes below the bandgap of the active material fro

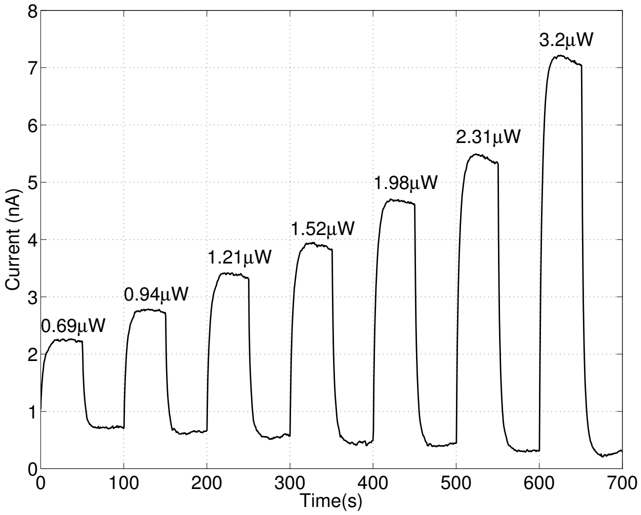

Figure 5.16: The responses of the Schottky diode under different illumination powers at zero bias with 50-second on/off periods and 350nm UV light. A decrease in dark current is observed from the response after illumination.

Schottky junction, it's not observed in the device shown here. This could be mainly due to the nonideal contact between aluminum and ZnO. Quantum dots are typical to have a lot of surface oxygen states due to abrupt stop of lattice growth and self-doping. These states could lead to changes in Fermi levels. Furthermore, the reaction between the aluminum and oxygen could also alter the surface states. Therefore, there might also be a barrier between aluminum and ZnO and the carriers could be trapped in the active material. This effect is further found in silver based devices, since silver is more reactive than aluminum and can greatly alter the surface states.

The time response of the device is also measured under zero bias at 350nm wavelength light and shown in Figure 5.16. Different light powers are used to illuminate the device at a 50-second interval to observe the device behavior. Consistent increase in photocurrent is observed when the device is illuminated under an increased light power. One interesting thing to keep in mind is that there's significant non-zero current even under zero bias. It could be possibly due to trapped carriers during synthesis and device making and the static electric charges. With the non-zero current, we also observe a decrease in dark current, especially after high intensity light illumination.

This partially confirms the long trapping states in the device. ZnO is subject to surface oxygen defects and oxygen adsorption/desorption processes [17, 70, 71]. Long time hole trapping could lower the Fermi level of the ZnO and thus increase the barrier of the metal/ZnO interface(Figure 5.17). This will result in an increase in barrier height and also induces degradation in device performance over long time UV exposure.

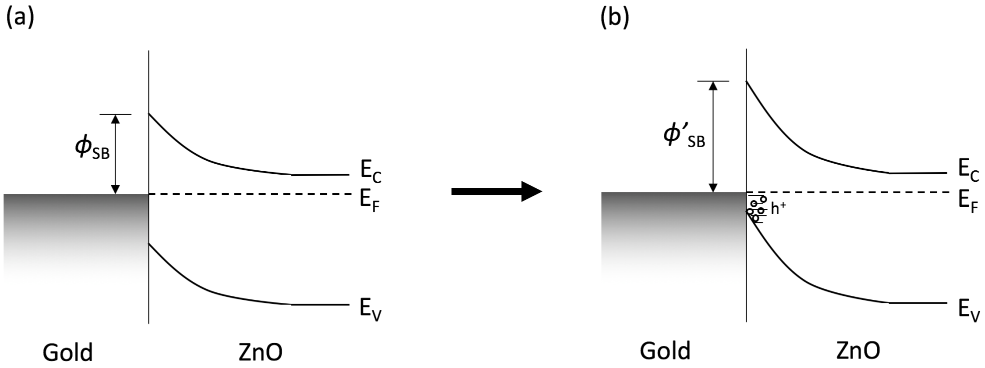

Figure 5.17: (a)The device structure of the Schottky diode; (b)Hole trapping induced barrier height increase at the interface.

The recovering of the dark current is observed through a long time measurement. The exponential increase is fitted to be

$$\begin{aligned} I &= I_C + A\exp\left(\frac{t}{\tau}\right) \\ &= 0.645 - 0.523\exp\left(-\frac{t}{129.28}\right), \end{aligned} \tag{5.3}$$

where A is the trapping cross-section related fitting parameter and τ is the discharging time, which is 129.28s in this case. I_C is supposed to be a constant dark current term. However, due to large amount to trapped carriers in the device, it decreases overtime. While the discharging time of C is much larger than the hole discharging time above, we can treat it as a constant.

5.3.2 With Molybdenum Oxide Layer

Thin molybdenum oxide(or trioxide to be more specific, MoO_3) [90] layers are commonly used as hole transporting layers for thin film solar cells [91] and light-emitting-diodes [92]. It has very high

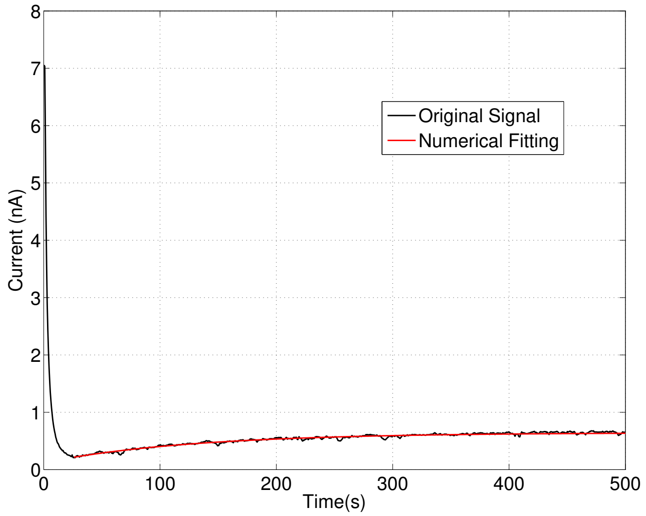

Figure 5.18: The recovering of the dark current, which is possibly due to releasing of trapped carriers. The black curve is the original signal that is fitted using an exponential function by the red curve.

electron affinity (as shown in Figure 5.19b) and can potentially be used to increase the barrier of the device and lead to better rectifying devices. The proposed device structure is shown in Figure 5.19a, with thicknesses of Au, MoO3 and Ag layers to be 20nm, 10-15nm and 100nm respectively. All these layers are deposited through thermal evaporation under a high vacuum level of $\sim 5\times 10^{-7}$ torr. There are also reported work on using MoO_3/metal/MoO_3 structure to fabricate transparent electrode [93], which also meets our needs. Silver is chosen mostly because of the relative ease for thermal evaporation, while aluminum dissolves tungsten boat pretty easily after melting at a high temperature.

A real device under probing is shown in Figure 5.20a. It has a look of a frying egg with the dark yellow part to be the gold/MoO_3 electrode and the “egg white” to be the silver back contact. The device is tested under a setup shown in Figure 5.20b with the gold electrode probed by a needle probe and the silver pad in touch on a grounded metal plate.

The current-voltage response of the device with and without light illumination is shown in Figure 5.21. The device appears to have a very good rectifying effect. By fitting the dark current

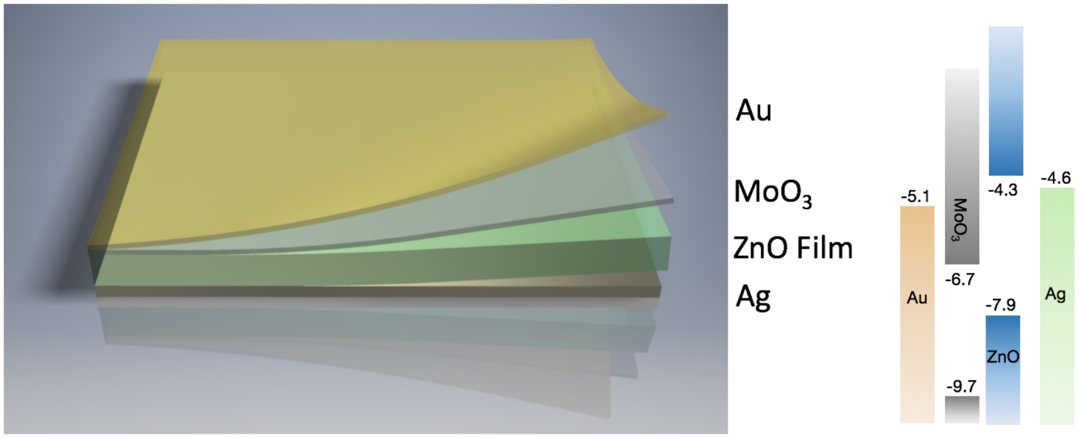

(a) (b)

Figure 5.19: (a)A schematic of the flexible photodetector device structure with a MoO$_3$ layer; (b)A work function diagram of the device.

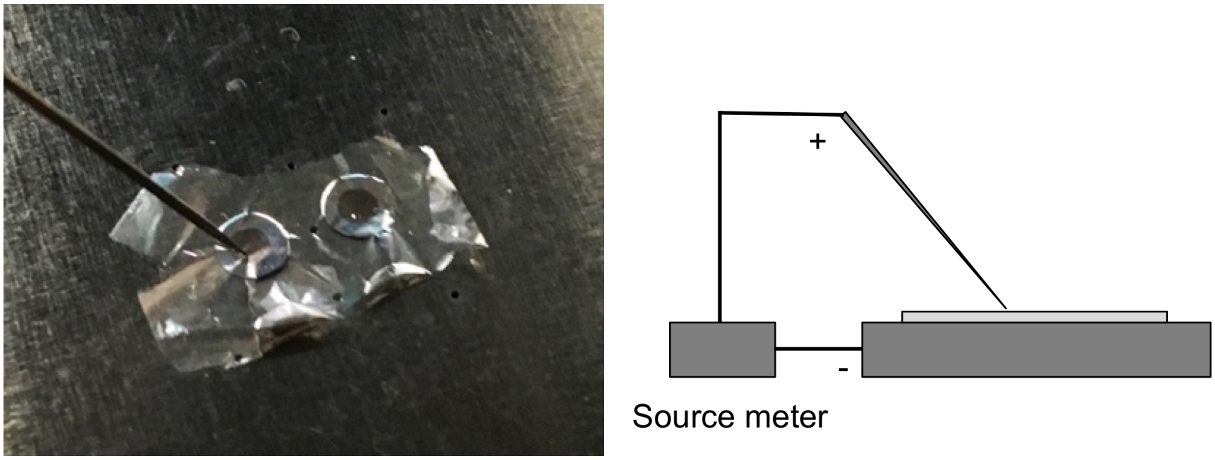

(a) (b)

Figure 5.20: (a)Real photodetectors under probing; (b)A schematic of the probing setup with the silver back contact attached to the grounding metal plate and the front gold transparent electrode probed by the probe.

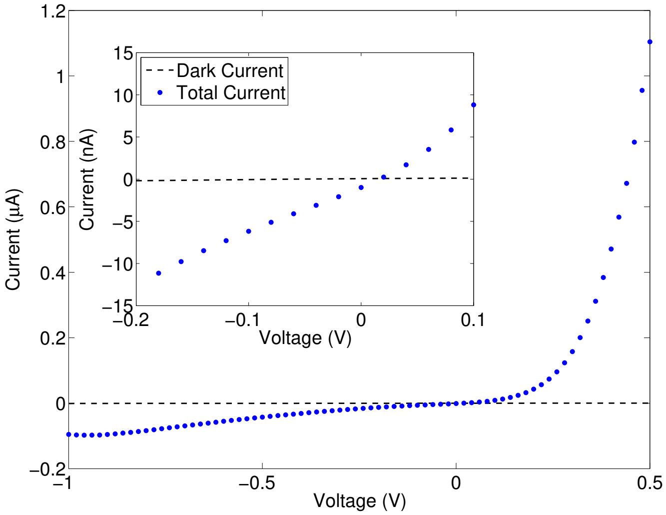

Figure 5.21: Current-voltage(I-V) curve of the device with and without UV illumination.

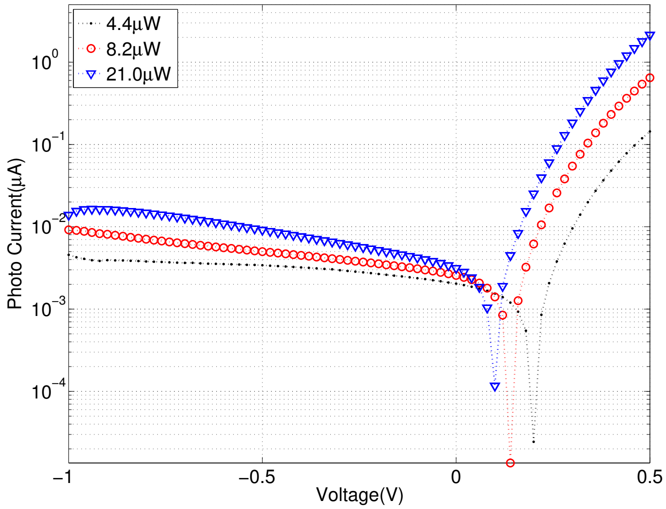

Figure 5.22: Photoresponses of the device under different illumination powers at 365nm.

with Schottky diode equation we get an ideality factor of $\sim$6.6, which is far from ideal due to interface states and probably also the influence of NFCs. The saturation current is $\sim 3.04\times10^{-9}$ A, which leads to a barrier height of $\sim$0.8eV. The device has an EQE of over 30% under 0.5V and $\sim$8% under -0.5V at 365nm wavelength light illumination. This is significantly higher then the gold/ZnO/aluminum device. We also tested the device under different illumination power, as shown in Figure 5.22. A saturation of the device is observed at higher power, possibly due to a saturated conduction band from high density electron excitation. Unlike the device shown in section 5.3.1, no response's observed under zero bias. This could be due to a barrier at the silver/ZnO interface. Silver is very reactive with oxygen and could alter the properties of the interface a lot. Darkened interfaces are observed after several days, which confirms the reaction between ZnO and silver and possibly leads to another Schottky barrier.

Chapter 6

CONCLUSIONS AND FUTURE WORK

6.1 Conclusions

The main idea of this thesis is to demonstrate that the active layer can be freestanded without supporting substrate and this can be applied to flexible optoelectronic devices. Nanocrystal quantum dots are used as the active material because it has very high optical yield and long carrier lifetime with suspended nonradiative processes, all due to strong three dimensional electron confinement. We found by using cellulose as the structuring material, we can make freestanding CQD-cellulose thin film for photodetection.

The first generation of device is fabricated on a tracing paper, which is a material we saw everyday. To lower the fabrication cost, we worked on inkjet printing of PEDOT:PSS electrodes on transparency films and obtained sub-100Ω/□ sheet resistance with $>85\%$ transmittance on 3-layer PEDOT:PSS. The porous structure in tracing paper enables us to incorporate CdSe CQDs into the paper structure. While the printed electrodes have big surface roughness and could short the device, the tracing paper layer also acts as an interspacing layer and overcomes the problem. We are able to get functional photoconductor out of a PEDOT:PSS/CdSe QD-tracing paper/PEDOT:PSS sandwich structure. However, due to large thickness and low porosity, the carrier transportation in such a layer is deteriorated. We also found that by bending the device, the performance increases, which indicates loose contacts between QDs. The lamination between three thick layers is also a problem. Thus we need to find a thinner and more porous interspacing layer, as well as better material deposition methods.

We then realized that some plant membranes are naturally more porous and thinner due to their functionality, such as nutrition transportation. Thus we looked into the commericially available material, reed membrane, which is commonly used as the flute vibration membrane. We also worked on the synthesis of ZnO QD, which is less toxic and has wide bandgap that could potentially lead to UV detection applications. We also changed to evaporation for depositing electrodes and received much better contacts. In order to have a faster device, we also introduced the Schottky diode structure with gold/ZnO QD-reed membrane/aluminum structure and received sub-second response time. $>3\%$ in external quantum efficiency photoresponse is also observed when operating under 350nm wavelength light. However, we found the natural membrane still has rough surface. The thickness of the membrane is also much larger than the common active material thickness and the porosity is determined.

Therefore, we decided to start from the cellulose membrane fabrication. We developed ultrathin ZnO QD-NFC composite membrane that has a thickness less than 1 μm and $>95\%$ transparency at visible light. By incorporating high density of ZnO QDs, we are able to make UV detectors on the membrane after depositing electrodes. Schottky diode structure is make possible with gold and aluminum acting as the electrodes. The device's able to function as a self-powered visible-blind UV detector with relatively fast response. A MoO_3 layer is also introduced to alter device performance and we saw pretty good rectifying effect with good EQEs performance under bias.

6.2 Future Work

The ZnO QD-NFC composite membrane opens up a lot more research possibilities other than the device we developed. This can be potentially applied to other optoelectronic devices with other functionality.

6.2.1 Transparent Devices

Being a transparent material, potentially we can fabricate transparent devices out of it. Other than aesthetic considerations, transparent devices can be used in a lot of applications such as windows, displays without the need of changing the underlying device structure. One easy way to do this is to fabricate lateral devices with better transparent electrodes. Graphene is a potential candidate for electrode choice thanks to its ultramobility and great transparency.

6.2.2 Solar Cell Coating

It's been proved that by engineering the optical haze of the nanopaper, the efficiency of the solar cell can be improved due to better diffusion of illuminating light. By incorporating CQDs with high optical yield, it's possible that the composite membrane can also work as solar concentrator by down-converting shorter wavelength light to longer wavelengths, with which solar cell has higher efficiency in absorbing them. Thus improving the solar cell performance.

6.2.3 Conformal Devices

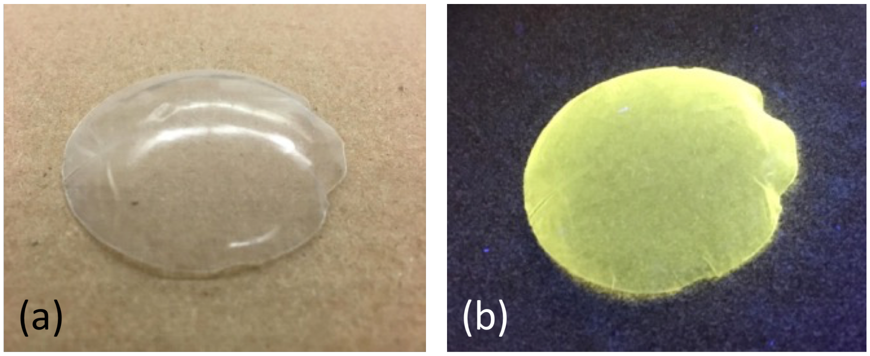

Figure 6.1: (a)A photo of a conformal paper made of ZnO QD-NFC composite material; (b)When the conformal paper's under UV excitation.

NFC gels are deconformable cause it's formed of nanosize cellulose fiber and full of solvent. Thus it can potentially be made into shapes other than flats. Figure 6.1 shows the conformal ZnO QD-NFC film we fabricated and it can be used as substrate for other devices.

BIBLIOGRAPHY

[1] Gunchul Shin, Inhwa Jung, Viktor Malyarchuk, Jizhou Song, Shuodao Wang, Heung Cho Ko, Yonggang Huang, Jeong Sook Ha, and John A. Rogers. Micromechanics and advanced designs for curved photodetector arrays in hemispherical electronic-eye cameras. *Small*, 6(7):851–856, 2010.

[2] Y. Yin and A. P. Alivisatos. Colloidal nanocrystal synthesis and the organic-inorganic interface. *Nature*, 437(7059):664–70, 2005.

[3] Robert W. Meulenberg, Jonathan R.I. Lee, Abraham Wolcott, Jin Z. Zhang, Louis J. Terminello, and Tony van Buuren. Determination of the exciton binding energy in cdse quantum dots. *ACS Nano*, 3(2):325–330, 2009.

[4] Peter Ramvall, Satoru Tanaka, Shintaro Nomura, Philippe Riblet, and Yoshinobu Aoyagi. Observation of confinement-dependent exciton binding energy of gan quantum dots. *Applied Physics Letters*, 73(8):1104–1106, 1998.

[5] M. C. Barr, J. A. Rowehl, R. R. Lunt, J. Xu, A. Wang, C. M. Boyce, S. G. Im, V. Bulovic, and K. K. Gleason. Direct monolithic integration of organic photovoltaic circuits on unmodified paper. *Advanced Materials*, 23(31):3499–3505, 2011.

[6] Liangbing Hu, Guangyuan Zheng, Jie Yao, Nian Liu, Ben Weil, Martin Eskilsson, Erdem Karabulut, Zhichao Ruan, Shanhui Fan, Jason T. Bloking, Michael D. McGehee, Lars Wagberg, and Yi Cui. Transparent and conductive paper from nanocellulose fibers. *Energy & Environmental Science*, 6(2):513–518, 2013.

[7] Qingjiang Sun, Y. Andrew Wang, Lin Song Li, Daoyuan Wang, Ting Zhu, Jian Xu, Chunhe Yang, and Yongfang Li. Bright, multicoloured light-emitting diodes based on quantum dots. *Nature Photonics*, 1(12):717–722, 2007.

[8] Alexander H Mueller, Melissa A Petruska, Marc Achermann, Donald J Werder, Elshan A Akhadov, Daniel D Koleske, Mark A Hoffbauer, and Victor I Klimov. Multicolor light-emitting diodes based on semiconductor nanocrystals encapsulated in gan charge injection layers. *Nano Letters*, 5(6):1039–1044, 2005.

[9] VL Colvin, MC Schlamp, A Paul Alivisatos, et al. Light-emitting-diodes made from cadmium selenide nanocrystals and a semiconducting polymer. *Nature*, 370(6488):354–357, 1994.

[10] Tae-Ho Kim, Kyung-Sang Cho, Eun Kyung Lee, Sang Jin Lee, Jungseok Chae, Jung Woo Kim, Do Hwan Kim, Jang-Yeon Kwon, Gehan Amaratunga, Sang Yoon Lee, Byoung Lyong Choi, Young Kuk, Jong Min Kim, and Kinam Kim. Full-colour quantum dot displays fabricated by transfer printing. *Nature Photonics*, 5(3):176–182, 2011. 10.1038/nphoton.2011.12.

[11] Wanli Ma, Joseph M Luther, Haimei Zheng, Yue Wu, and A Paul Alivisatos. Photovoltaic devices employing ternary pbs x se1-x nanocrystals. *Nano letters*, 9(4):1699–1703, 2009.

[12] Steven A McDonald, Gerasimos Konstantatos, Shiguo Zhang, Paul W Cyr, Ethan JD Klem, Larissa Levina, and Edward H Sargent. Solution-processed pbs quantum dot infrared photodetectors and photovoltaics. *Nature materials*, 4(2):138–142, 2005.

[13] Wendy U Huynh, Janke J Dittmer, and A Paul Alivisatos. Hybrid nanorod-polymer solar cells. *science*, 295(5564):2425–2427, 2002.

[14] Armin Fischer, Lisa Rollny, Jun Pan, Graham H Carey, Susanna M Thon, Sjoerd Hoogland, Oleksandr Voznyy, David Zhitomirsky, Jin Young Kim, Osman M Bakr, et al. Directly deposited quantum dot solids using a colloidally stable nanoparticle ink. *Advanced Materials*, 25(40):5742–5749, 2013.

[15] Nan Liu, He Tian, Gregor Schwartz, Jeffrey B-H Tok, Tian-Ling Ren, and Zhenan Bao. Large-area, transparent, and flexible infrared photodetector fabricated using pn junctions formed by n-doping chemical vapor deposition grown graphene. *Nano letters*, 14(7):3702–3708, 2014.

[16] Zhiwei Gao, Weifeng Jin, Yu Zhou, Yu Dai, Bin Yu, Chu Liu, Wanjin Xu, Yanping Li, Hailin Peng, Zhongfan Liu, et al. Self-powered flexible and transparent photovoltaic detectors based on cdse nanobelt/graphene schottky junctions. *Nanoscale*, 5(12):5576–5581, 2013.

[17] Yizheng Jin, Jianpu Wang, Baoquan Sun, James C Blakesley, and Neil C Greenham. Solution-processed ultraviolet photodetectors based on colloidal zno nanoparticles. *Nano letters*, 8(6):1649–1653, 2008.

[18] Rui Dong, Cheng Bi, Qingfeng Dong, Fawen Guo, Yongbo Yuan, Yanjun Fang, Zhengguo Xiao, and Jinsong Huang. An ultraviolet-to-nir broad spectral nanocomposite photodetector with gain. *Advanced Optical Materials*, 2(6):549–554, 2014.

[19] Dmitri V Talapin and Christopher B Murray. Pbse nanocrystal solids for n-and p-channel thin film field-effect transistors. *Science*, 310(5745):86–89, 2005.

[20] AL Roest, JJ Kelly, D Vanmaekelbergh, and EA Meulenkamp. Staircase in the electron mobility of a zno quantum dot assembly due to shell filling. *Physical review letters*, 89(3):036801, 2002.

[21] Al L Efros and Al L Efros. Interband absorption of light in a semiconductor sphere. *Soviet Physics Semiconductors-Ussr*, 16(7):772–775, 1982.

[22] Sergey V Gaponenko. *Optical properties of semiconductor nanocrystals*, volume 23. Cambridge university press, 1998.

[23] CBea Murray, David J Norris, and Moungi G Bawendi. Synthesis and characterization of nearly monodisperse cde (e= sulfur, selenium, tellurium) semiconductor nanocrystallites. *Journal of the American Chemical Society*, 115(19):8706–8715, 1993.

[24] S Corni, M Braskén, M Lindberg, J Olsen, and D Sundholm. Size dependence of the electron-hole recombination rates in semiconductor quantum dots. *Physical Review B*, 67(4):045313, 2003.

[25] Alberto Franceschetti and Alex Zunger. Direct pseudopotential calculation of exciton coulomb and exchange energies in semiconductor quantum dots. *Physical review letters*, 78(5):915, 1997.

[26] Victor K LaMer and Robert H Dinegar. Theory, production and mechanism of formation of monodispersed hydrosols. *Journal of the American Chemical Society*, 72(11):4847–4854, 1950.

[27] Christopher B Murray, CR Kagan, and MG Bawendi. Synthesis and characterization of monodisperse nanocrystals and close-packed nanocrystal assemblies. *Annual Review of Materials Science*, 30(1):545–610, 2000.

[28] Robert J Moon. Nanomaterials in the forest products industry. 2008.

[29] Hongli Zhu, Zhiqiang Fang, Colin Preston, Yuanyuan Li, and Liangbing Hu. Transparent paper: fabrications, properties, and device applications. *Energy & Environmental Science*, 7(1):269–287, 2014.

[30] Franklin W Herrick, RONALD L Casebier, J KELVIN Hamilton, and KAREN R Sandberg. Microfibrillated cellulose: morphology and accessibility. In *J. Appl. Polym. Sci.: Appl. Polym. Symp.;(United States)*, volume 37. ITT Rayonier Inc., Shelton, WA, 1983.

[31] Akira Isogai and Yumiko Kato. Preparation of polyuronic acid from cellulose by tempo-mediated oxidation. *Cellulose*, 5(3):153–164, 1998.

[32] Akira Isogai, Tsuguyuki Saito, and Hayaka Fukuzumi. Tempo-oxidized cellulose nanofibers. *Nanoscale*, 3(1):71–85, 2011.

[33] Alain Dufresne. Nanocellulose: a new ageless bionanomaterial. *Materials Today*, 16(6):220–227, 2013.

[34] Marielle Henriksson, Lars A Berglund, Per Isaksson, Tom Lindstrom, and Takashi Nishino. Cellulose nanopaper structures of high toughness. *Biomacromolecules*, 9(6):1579–1585, 2008.

[35] Robert J Moon, Ashlie Martini, John Nairn, John Simonsen, and Jeff Youngblood. Cellulose nanomaterials review: structure, properties and nanocomposites. *Chemical Society Reviews*, 40(7):3941–3994, 2011.

[36] Zhe Gui, Hongli Zhu, Eleanor Gillette, Xiaogang Han, Gary W Rubloff, Liangbing Hu, and Sang Bok Lee. Natural cellulose fiber as substrate for supercapacitor. *ACS nano*, 7(7):6037–6046, 2013.

[37] Hongli Zhu, Zheng Jia, Yuchen Chen, Nicholas Weadock, Jiayu Wan, Oeyvind Vaaland, Xiaogang Han, Teng Li, and Liangbing Hu. Tin anode for sodium-ion batteries using natural wood fiber as a mechanical buffer and electrolyte reservoir. *Nano letters*, 13(7):3093–3100, 2013.

[38] Elvira Fortunato, Nuno Correia, Pedro Barquinha, Luís Pereira, Gonçalo Gonçalves, and Rodrigo Martins. High-performance flexible hybrid field-effect transistors based on cellulose fiber paper. *IEEE Electron Device Letters*, 29(9):988–990, 2008.

[39] Peter Andersson, David Nilsson, Per-Olof Svensson, Miaoxiang Chen, Anna Malmström, Tommi Remonen, Thomas Kugler, and Magnus Berggren. Active matrix displays based on all-organic electrochemical smart pixels printed on paper. *Advanced Materials*, 14(20):1460–1464, 2002.

[40] Jin-Young Kim, Shang Hyeun Park, Taewon Jeong, Min Jong Bae, Sunjin Song, Jeonghee Lee, In Taek Han, Donggeun Jung, and SeGi Yu. Paper as a substrate for inorganic powder electroluminescence devices. *IEEE Transactions on Electron Devices*, 57(6):1470–1474, 2010.

[41] Daniel Tobjörk and Ronald Österbacka. Paper electronics. *Advanced Materials*, 23(17):1935–1961, 2011.

[42] Yuanyuan Song, Yaoquan Jiang, Liyi Shi, Shaomei Cao, Xin Feng, Miao Miao, and Jianhui Fang. Solution-processed assembly of ultrathin transparent conductive cellulose nanopaper embedding agnws. *Nanoscale*, 7(32):13694–13701, 2015.

[43] Hirotaka Koga, Masaya Nogi, Natsuki Komoda, Thi Thi Nge, Tohru Sugahara, and Katsuaki Suganuma. Uniformly connected conductive networks on cellulose nanofiber paper for transparent paper electronics. *NPG Asia Mater*, 6(3):e93, 2014.

[44] Jia Huang, Hongli Zhu, Yuchen Chen, Colin Preston, Kathleen Rohrbach, John Cumings, and Liangbing Hu. Highly transparent and flexible nanopaper transistors. *Acs Nano*, 7(3):2106–2113, 2013.

[45] Eden Morales-Narváez, Hamed Golmohammadi, Tina Naghdi, Hossein Yousefi, Uliana Kostiv, Daniel Horák, Nahid Pourreza, and Arben Merkoçi. Nanopaper as an optical sensing platform. *ACS nano*, 9(7):7296–7305, 2015.

[46] Richard T Olsson, MAS Azizi Samir, German Salazar-Alvarez, Liubov Belova, Valter Ström, Lars A Berglund, O Ikkala, J Nogues, and Ulf W Gedde. Making flexible magnetic aerogels and stiff magnetic nanopaper using cellulose nanofibrils as templates. *Nature nanotechnology*, 5(8):584–588, 2010.

[47] Yuanyuan Li, Hongli Zhu, Hongbo Gu, Hongqi Dai, Zhiqiang Fang, Nicholas J Weadock, Zhanhu Guo, and Liangbing Hu. Strong transparent magnetic nanopaper prepared by immobilization of fe_3o_4 nanoparticles in a nanofibrillated cellulose network. *Journal of Materials Chemistry A*, 1(48):15278–15283, 2013.

[48] Juan Xue, Fei Song, Xue-wu Yin, Xiu-li Wang, and Yu-zhong Wang. Let it shine: a transparent and photoluminescent foldable nanocellulose/quantum dot paper. *ACS applied materials & interfaces*, 7(19):10076–10079, 2015.

[49] Zhiqiang Fang, Hongli Zhu, Yongbo Yuan, Dongheon Ha, Shuze Zhu, Colin Preston, Qingxia Chen, Yuanyuan Li, Xiaogang Han, Seongwoo Lee, et al. Novel nanostructured paper with ultrahigh transparency and ultrahigh haze for solar cells. *Nano letters*, 14(2):765–773, 2014.

[50] Hongli Zhu, Zhiqiang Fang, Zhu Wang, Jiaqi Dai, Yonggang Yao, Fei Shen, Colin Preston, Wenxin Wu, Peng Peng, Nathaniel Jang, et al. Extreme light management in mesoporous wood cellulose paper for optoelectronics. *ACS nano*, 10(1):1369–1377, 2015.

[51] L. Groenendaal, F. Jonas, D. Freitag, H. Pielartzik, and J. R. Reynolds. Poly(3,4-ethylenedioxythiophene) and its derivatives: Past, present, and future. *Advanced Materials*, 12(7):481–494, 2000.

[52] Zhong Chen, Brian Cotterell, and Wei Wang. The fracture of brittle thin films on compliant substrates in flexible displays. *Engineering Fracture Mechanics*, 69(5):597–603, 2002.

[53] Chavis Srichan, Thitirat Saikrajang, Tanom Lomas, Apichai Jomphoak, Thitima Maturos, Disayut Phokaratkul, Teerakiat Kerdcharoen, and Adisorn Tuantranont. Inkjet printing pedot: Pss using desktop inkjet printer. In *Electrical Engineering/Electronics, Computer, Telecommunications and Information Technology, 2009. ECTI-CON 2009. 6th International Conference on*, volume 1, pages 465–468. IEEE, 2009.

[54] S. Ummartyotin, J. Juntaro, C. Wu, M. Sain, and H. Manuspiya. Deposition of pedot: Pss nanoparticles as a conductive microlayer anode in oleds device by desktop inkjet printer. *Journal of Nanomaterials*, 2011:1–7, 2011.

[55] Michaela Böberl, Maksym V Kovalenko, Stefan Gamerith, Emil JW List, and Wolfgang Heiss. Inkjet-printed nanocrystal photodetectors operating up to 3 μm wavelengths. *Advanced Materials*, 19(21):3574–3578, 2007.

[56] Seung H Ko, Heng Pan, Costas P Grigoropoulos, Christine K Luscombe, Jean MJ Fréchet, and Dimos Poulikakos. All-inkjet-printed flexible electronics fabrication on a polymer substrate by low-temperature high-resolution selective laser sintering of metal nanoparticles. *Nanotechnology*, 18(34):345202, 2007.

[57] Krisztián Kordás, Tero Mustonen, Géza Tóth, Heli Jantunen, Marja Lajunen, Caterina Soldano, Saikat Talapatra, Swastik Kar, Robert Vajtai, and Pulickel M Ajayan. Inkjet printing of electrically conductive patterns of carbon nanotubes. *Small*, 2(8-9):1021–1025, 2006.

[58] Yuka Yoshioka and Ghassan E. Jabbour. Desktop inkjet printer as a tool to print conducting polymers. *Synthetic Metals*, 156(11-13):779–783, 2006.

[59] L Hu, DS Hecht, and G Grüner. Percolation in transparent and conducting carbon nanotube networks. *Nano Letters*, 4(12):2513–2517, 2004.

[60] Jingda Wu and Lih Y Lin. Flexible thin-film nanocrystal quantum dot photodetectors on unmodified transparency films. In *IEEE Photonics Conference 2012*, 2012.

[61] Claudia Pacholski, Andreas Kornowski, and Horst Weller. Self-assembly of zno: from nanodots to nanorods. *Angewandte Chemie International Edition*, 41(7):1188–1191, 2002.

[62] Xun Wang, Jing Zhuang, Qing Peng, and Yadong Li. A general strategy for nanocrystal synthesis. *Nature*, 437(7055):121–124, 2005.

[63] Dianyi Liu and Timothy L Kelly. Perovskite solar cells with a planar heterojunction structure prepared using room-temperature solution processing techniques. *Nature photonics*, 8(2):133–138, 2014.

[64] Ranjani Viswanatha, Sameer Sapra, B Satpati, PV Satyam, BN Dev, and DD Sarma. Understanding the quantum size effects in zno nanocrystals. *Journal of Materials Chemistry*, 14(4):661–668, 2004.

[65] Dmitri V Talapin, Jong-Soo Lee, Maksym V Kovalenko, and Elena V Shevchenko. Prospects of colloidal nanocrystals for electronic and optoelectronic applications. *Chemical reviews*, 110(1):389–458, 2009.

[66] Simon M Sze and Kwok K Ng. *Physics of semiconductor devices*. John wiley & sons, 2006.

[67] Leonard J Brillson and Yicheng Lu. Zno schottky barriers and ohmic contacts. *Journal of Applied Physics*, 109(12):121301, 2011.

[68] Marcus C Newton, Steven Firth, and Paul A Warburton. Zno tetrapod schottky photodiodes. *Applied physics letters*, 89(7):072104, 2006.

[69] Zhaolin Yuan. A photodiode with high rectification ratio and low turn-on voltage based on zno nanoparticles and subpc planar heterojunction. *Physica E: Low-dimensional Systems and Nanostructures*, 56:160–164, 2014.

[70] Kihyun Keem, Hyunsuk Kim, Gyu-Tae Kim, Jong Soo Lee, Byungdon Min, Kyoungah Cho, Man-Young Sung, and Sangsig Kim. Photocurrent in zno nanowires grown from au electrodes. *Applied Physics Letters*, 84(22):4376–4378, 2004.

[71] Hannes Kind, Haoquan Yan, Benjamin Messer, Matthew Law, Peidong Yang, et al. Nanowire ultraviolet photodetectors and optical switches. *Advanced materials*, 14(2):158, 2002.

[72] Wei Tian, Chao Zhang, Tianyou Zhai, Song-Lin Li, Xi Wang, Jiangwei Liu, Xiao Jie, Dequan Liu, Meiyong Liao, Yasuo Koide, et al. Flexible ultraviolet photodetectors with broad photoresponse based on branched zns-zno heterostructure nanofilms. *Advanced Materials*, 26(19):3088–3093, 2014.

[73] Suo Bai, Weiwei Wu, Yong Qin, Nuanyang Cui, Dylan J Bayerl, and Xudong Wang. High-performance integrated zno nanowire uv sensors on rigid and flexible substrates. *Advanced Functional Materials*, 21(23):4464–4469, 2011.

[74] Zhenxing Wang, Xueying Zhan, Yajun Wang, Safdar Muhammad, Ying Huang, and Jun He. A flexible uv nanosensor based on reduced graphene oxide decorated zno nanostructures. *Nanoscale*, 4(8):2678–2684, 2012.

[75] Zhuoran Wang, Heng Wang, Bin Liu, Wenzhe Qiu, Jun Zhang, Sihan Ran, Hongtao Huang, Jing Xu, Hongwei Han, Di Chen, et al. Transferable and flexible nanorod-assembled tio2 cloths for dye-sensitized solar cells, photodetectors, and photocatalysts. *ACS nano*, 5(10):8412–8419, 2011.

[76] Wei Tian, Chao Zhang, Tianyou Zhai, Song-Lin Li, Xi Wang, Meiyong Liao, Kazuhito Tsukagoshi, Dmitri Golberg, and Yoshio Bando. Flexible sno 2 hollow nanosphere film based high-performance ultraviolet photodetector. *Chemical Communications*, 49(36):3739–3741, 2013.

[77] Lu Ren, Tingting Tian, Yuanzhi Li, Jianguo Huang, and Xiujian Zhao. High-performance uv photodetection of unique zno nanowires from zinc carbonate hydroxide nanobelts. *ACS applied materials & interfaces*, 5(12):5861–5867, 2013.

[78] Zhiwen Jin, Liang Gao, Qing Zhou, and Jizheng Wang. High-performance flexible ultraviolet photoconductors based on solution-processed ultrathin zno/au nanoparticle composite films. *Scientific reports*, 4, 2014.

[79] Yanru Xie, Lin Wei, Guodong Wei, Qinghao Li, Dong Wang, Yanxue Chen, Shishen Yan, Guolei Liu, Liangmo Mei, and Jun Jiao. A self-powered uv photodetector based on tio2 nanorod arrays. *Nanoscale research letters*, 8(1):1–6, 2013.

[80] Junjie Qi, Xiaofeng Hu, Zengze Wang, Xin Li, Wang Liu, and Yue Zhang. A self-powered ultraviolet detector based on a single zno microwire/p-si film with double heterojunctions. *Nanoscale*, 6(11):6025–6029, 2014.

[81] Onkar Game, Upendra Singh, Tanya Kumari, Arun Banpurkar, and Satishchandra Ogale. Zno (n)–spiro-meotad hybrid photodiode: an efficient self-powered fast-response uv (visible) photosensor. *Nanoscale*, 6(1):503–513, 2014.

[82] Zhiming Bai, Xiang Chen, Xiaoqin Yan, Xin Zheng, Zhuo Kang, and Yue Zhang. Self-powered ultraviolet photodetectors based on selectively grown zno nanowire arrays with thermal tuning performance. *Physical Chemistry Chemical Physics*, 16(20):9525–9529, 2014.

[83] Sabina M Hatch, Joe Briscoe, and Steve Dunn. A self-powered zno-nanorod/cuscn uv photodetector exhibiting rapid response. *Advanced Materials*, 25(6):867–871, 2013.

[84] Hugh L Zhu, Wallace CH Choy, Wei EI Sha, and Xingang Ren. Photovoltaic mode ultraviolet organic photodetectors with high on/off ratio and fast response. *Advanced Optical Materials*, 2(11):1082–1089, 2014.

[85] Pierre-Gilles De Gennes. Wetting: statics and dynamics. *Reviews of modern physics*, 57(3):827, 1985.

[86] Malcolm E Schrader. Young-dupre revisited. *Langmuir*, 11(9):3585–3589, 1995.

[87] Andrew Carlson, Audrey M Bowen, Yonggang Huang, Ralph G Nuzzo, and John A Rogers. Transfer printing techniques for materials assembly and micro/nanodevice fabrication. *Advanced Materials*, 24(39):5284–5318, 2012.

[88] Wei Zheng and Zhao Ya-Pu. Experimental investigation of the velocity effect on adhesion forces with an atomic force microscope. *Chinese Physics Letters*, 21(4):616, 2004.

[89] Olivier Noel, Pierre-Emmanuel Mazeran, and Hussein Nasrallah. Sliding velocity dependence of adhesion in a nanometer-sized contact. *Physical review letters*, 108(1):015503, 2012.

[90] David O Scanlon, Graeme W Watson, DJ Payne, GR Atkinson, RG Egdell, and DSL Law. Theoretical and experimental study of the electronic structures of moo3 and moo2. *The Journal of Physical Chemistry C*, 114(10):4636–4645, 2010.

[91] Mark T Greiner, Lily Chai, Michael G Helander, Wing-Man Tang, and Zheng-Hong Lu. Metal/metal-oxide interfaces: how metal contacts affect the work function and band structure of moo3. *Advanced Functional Materials*, 23(2):215–226, 2013.

[92] QY Bao, JP Yang, YQ Li, and JX Tang. Electronic structures of moo3-based charge generation layer for tandem organic light-emitting diodes. *Appl Phys Lett*, 97:063303, 2010.

[93] Linda Cattin, M Morsli, F Dahou, S Yapi Abe, A Khelil, and JC Bernède. Investigation of low resistance transparent moo 3/ag/moo 3 multilayer and application as anode in organic solar cells. *Thin Solid Films*, 518(16):4560–4563, 2010.

VITA

Jingda Wu was born in Ningbo, China. He received his B.S. degree in Optics/Physics from Sun Yat-sen University, which is located at Guangdong, China, in 2011. He worked on semiconductor spintronics during his undergraduate and studied spin relaxation and diffusion mechanisms using time-resolved pump-probe experiment. He started his Ph.D. study at the University of Washington at Seattle in Electrical Engineering program in 2011. Since then, he has worked on projects involving flexible quantum dot photodetection, optical tweezers and MEMS mass sensing resonator. His research interests include experimental quantum physics, light-matter interaction, novel materials and nanodevice.